SANDIA REPORT
SAND2020-9914X
Printed September 2020

Sandia National Laboratories

Coupling of Laminar-Turbulent Transition with RANS Computational Fluid Dynamics

Neal P. Bitter, Alec Kucala, Jeff Fike, Michael Krygier, and Ross Wagnild

Prepared by
Sandia National Laboratories
Albuquerque, New Mexico 87185
Livermore, California 94550

Issued by Sandia National Laboratories, operated for the United States Department of Energy by National Technology & Engineering Solutions of Sandia, LLC.

NOTICE: This report was prepared as an account of work sponsored by an agency of the United States Government. Neither the United States Government, nor any agency thereof, nor any of their employees, nor any of their contractors, subcontractors, or their employees, make any warranty, express or implied, or assume any legal liability or responsibility for the accuracy, completeness, or usefulness of any information, apparatus, product, or process disclosed, or represent that its use would not infringe privately owned rights. Reference herein to any specific commercial product, process, or service by trade name, trademark, manufacturer, or otherwise, does not necessarily constitute or imply its endorsement, recommendation, or favoring by the United States Government, any agency thereof, or any of their contractors or subcontractors. The views and opinions expressed herein do not necessarily state or reflect those of the United States Government, any agency thereof, or any of their contractors.

Printed in the United States of America. This report has been reproduced directly from the best available copy.

Available to DOE and DOE contractors from

U.S. Department of Energy
Office of Scientific and Technical Information
P.O. Box 62
Oak Ridge, TN 37831

Telephone: (865) 576-8401
Facsimile: (865) 576-5728
E-Mail: reports@osti.gov
Online ordering: http://www.osti.gov/scitech

Available to the public from

U.S. Department of Commerce
National Technical Information Service
5301 Shawnee Road
Alexandria, VA 22312

Telephone: (800) 553-6847
Facsimile: (703) 605-6900
E-Mail: orders@ntis.gov
Online order: https://classic.ntis.gov/help/order-methods

ABSTRACT

This project combines several new concepts to create a boundary layer transition prediction capability that is suitable for analyzing modern hypersonic flight vehicles. The first new concept is the use of “optimization” methods to detect the hydrodynamic instabilities that cause boundary layer transition; the use of this method removes the need for many limiting assumptions of other methods and enables quantification of the interactions between boundary layer instabilities and the flow field imperfections that generate them. The second new concept is the execution of transition analysis within a conventional hypersonics CFD code, using the same mesh and numerical schemes for the transition analysis and the laminar flow simulation. This feature enables rapid execution of transition analysis with less user oversight required and no interpolation steps needed.

ACKNOWLEDGMENTS

This research was funded by Sandia National Laboratories Laboratory Directed Research and Development (LDRD) program. Sandia National Laboratories is a multimission laboratory managed and operated by National Technology & Engineering Solutions of Sandia, LLC, a wholly owned subsidiary of Honeywell International Inc., for the U.S. Department of Energy's National Nuclear Security Administration under contract DE-NA0003525.

CONTENTS

LIST OF FIGURES

LIST OF TABLES

EXECUTIVE SUMMARY

Throughout the history of hypersonics flight research, the transition from laminar to turbulent flow has been a frustrating source of uncertainty in re-entry vehicle design. Vehicles flying at hypersonic speeds undergo enormous heating loads that must be mitigated using a Thermal Protection System (TPS) to prevent structural damage. If the flow past the vehicle is turbulent, the heating rate can be 4-10 times larger than that of laminar flow, thus the points along the trajectory at which transition to turbulence takes place are often first-order design considerations. The location along the surface of the vehicle at which transition occurs is also important to predict, since the heating rate generally features a local maximum during the transition from laminar to turbulent flow, and vibrational loads are also most intense in this region. While existing computational fluid dynamics (CFD) models are adequate for simulating either fully laminar or fully turbulent attached flow, they are not capable of predicting transition to turbulence. There are currently no viable computational tools that deliver acceptable a priori predictions of transition for hypersonic flight.

In the past, engineering predictions of boundary layer transition have usually been made using empirical correlations that are calibrated against a large body of historical flight data. These correlations are useful when designing vehicles similar to those that have been flown before, but are not predictive when the vehicle geometry, TPS materials, or trajectory are changed. Additionally, correlations obtained using ground-based wind tunnels do not extrapolate to the flight environment, so the development of new correlations for new applications would require expensive flight tests. Because of their reliance on correlations, current transition predictions have large uncertainties which demand that costly margins be included in the design of the entire system. To reduce these margins and minimize the number of costly flight tests, future missions will require that transition be predicted a priori on the basis of the fluid mechanics rather than using empirical correlations. This project proposes a new computational method that can predict and model laminar-turbulent boundary layer transition on complex re-entry systems. The new method will be closely coupled with an existing hypersonic CFD solver so that the solver can predict transition and simulate the laminar, transitional, and turbulent regions of the flow in a single analysis. The new computational method offers numerous advantages over current practice and other competing technologies. The largest benefit is that the new method is based on physical solutions of the compressible Navier-Stokes equations, rather than on empirical correlations. This means that the new approach can be used to analyze new geometries, materials, and trajectories that are radically different from those flown previously. Although other competing technologies exist, they have generally not been useful for hypersonic vehicle design because they make unacceptable simplifying assumptions, they can analyze only a small subset of the possible mechanisms of transition to turbulence, and the analysis is cumbersome and time consuming. The new proposed computational method solves all of these problems. It avoids the simplifying

assumptions invoked by other methods, it accounts for all mechanisms of transition to turbulence, and it is tightly integrated with a hypersonic CFD solver.

This project takes the first steps towards delivering a predictive tool that can simultaneously simulate laminar, transitional, and turbulent regions of the flow. If successful, this technology will be an enormous step forward in capability, both for modeling re-entry systems (including future NW systems and boost-glide vehicles) and for modeling turbulent transition in other applications across Sandia's mission space.

1. INTRODUCTION

1.1. Project Overview

Throughout the history of hypersonics flight research, the transition from laminar to turbulent flow has been a frustrating source of uncertainty in re-entry vehicle design. Vehicles flying at hypersonic speeds undergo enormous heating loads that must be mitigated using a Thermal Protection System (TPS) to prevent structural damage. If the flow past the vehicle is turbulent, the heating rate can be 4-10 times larger than that of laminar flow, thus the points along the trajectory at which transition to turbulence takes place are often first-order design considerations. The location along the surface of the vehicle at which transition occurs is also important to predict, since the heating rate generally features a local maximum during the transition from laminar to turbulent flow, and vibrational loads are also most intense in this region. While existing computational fluid dynamics (CFD) models are adequate for simulating either fully laminar or fully turbulent attached flow, they are not capable of predicting transition to turbulence. There are currently no viable computational tools that deliver acceptable a priori predictions of transition for hypersonic flight.

In the past, engineering predictions of boundary layer transition have usually been made using empirical correlations that are calibrated against a large body of historical flight data. These correlations are useful when designing vehicles similar to those that have been flown before, but are not predictive when the vehicle geometry, TPS materials, or trajectory are changed. Additionally, correlations obtained using ground-based wind tunnels do not extrapolate to the flight environment, so the development of new correlations for new applications would require expensive flight tests. Because of their reliance on correlations, current transition predictions have large uncertainties which demand that costly margins be included in the design of the entire system. To reduce these margins and minimize the number of costly flight tests, future missions will require that transition be predicted a priori on the basis of the fluid mechanics rather than using empirical correlations.

In this project, a new computational method is developed that can predict and model laminar-turbulent boundary layer transition on complex re-entry systems. The new method will be integrated into an existing hypersonic CFD solver so future development will allow the solver to predict transition and simulate the laminar, transitional, and turbulent regions of the flow in a single analysis. The new computational method offers numerous advantages over current practice and other competing technologies [2, 5, 12–14]. The largest benefit is that the new method is based on physical solutions of the compressible Navier-Stokes equations, rather than on empirical correlations. This means that the new approach can be used to analyze new geometries, materials, and trajectories that are radically different from those flown previously. Although other competing technologies exist, they have generally not been useful for hypersonic vehicle design

because they make unacceptable simplifying assumptions, they can analyze only a small subset of the possible mechanisms of transition to turbulence, and/or the analysis is cumbersome and time consuming. The new proposed computational method solves all of these problems. It avoids the simplifying assumptions invoked by other methods, it accounts for all mechanisms of transition to turbulence, and it is tightly integrated with a hypersonic CFD solver.

1.2. Overview of the method

The goal of this project is a new computational method that can predict and model laminar-turbulent transition in hypersonic boundary layers from within a CFD solver. The start of transition is usually defined as the locus of points on the surface of the vehicle at which the heat flux begins to increase above the laminar value. In general, the start of transition varies around the circumference of the vehicle; for example, transition could begin further forward on the windward side of a pitched vehicle compared to the lee side. Additionally, different physical mechanisms can be responsible for transition at different locations, so the computational method must be able to simultaneously account for all of these different mechanisms.

1.2.1. Prediction of the Transition Location

As has already been discussed, it is essential that future predictions of boundary layer transition be made on the basis of the physical mechanisms involved, rather than on empirical correlations. At flight conditions, transition to turbulence is understood to take place by the following process. Small disturbances are inevitably introduced into the flow from a variety of sources including atmospheric velocity and temperature fluctuations, sound waves, impacts from particulate matter, and irregularities on the surface of the flight body. At low Reynolds numbers, these small disturbances decay away and the flow remains laminar. For sufficiently high Reynolds numbers, the disturbances amplify and grow until they are large enough to cause the flow to break down into turbulence. This project proposes a new approach to transition prediction in which an optimization problem is solved to identify the form of disturbance that has the greatest potential to trigger transition to turbulence. The solution of the optimization problem also yields the amount that the disturbance will grow, which is then used to predict where transition to turbulence begins. It should be noted that this transition prediction method currently relies on an empirically measured breakdown amplitude, thus is not entirely predictive. This would make the method semi-empirical, similar to the linear stability analysis in competing methods [5, 12–14], where the transition prediction relies on anchoring transition to a relative growth of disturbances. While this distinction may seem subtle, the power of the current method will be described in the demonstration shown below.

To frame laminar-turbulent transition as an optimization problem, one first considers the source of the disturbances such as atmospheric velocity and temperature fluctuations or sound waves. The average amplitude of these sources is usually known or can be estimated, but the fluctuations are stochastic in nature and take on many different orientations, wavelengths, frequencies, and waveforms. The goal of the optimization problem is to find the "most dangerous" form of

disturbance which has the greatest potential to trigger transition. The optimization algorithm searches among all possible disturbances of known initial amplitude to find the disturbance that gains the most energy as it travels through the laminar region of the boundary layer.

The novelty of this approach is that the optimization problem described above can be solved using the numerical schemes already contained in standard aerodynamics CFD solvers. The CFD solver is adapted to solve an auxiliary set of equations alongside the usual equations of fluid mechanics. The key enabling technology is that the time marching scheme associated with the standard CFD solver can be harnessed to solve optimization problems of this type. Some of the theoretical groundwork for such an approach has already been laid by other researchers [1, 11, 19], but much work remains to convert this basic concept into a predictive tool. Development of this technology has only recently begun, since the requisite advances in linear algebra and computing power have only been made in the last decade or so. The work of other researchers has so far been limited to academic contexts and has only been applied to simple model problems. Furthermore, this approach has never been used to make actual predictions of transition to turbulence, and consequently this approach has not been subjected to experimental validation [10]. This project will build on and refine the available conceptual framework to deliver an engineering capability that has been validated against experiments.

Another key benefit of this method is that it is agnostic to the mechanism that causes transition. It is well-known that transition to turbulence can be caused by numerous mechanisms, such as Tollmien-Schlichting waves, "2nd mode" waves, and crossflow instabilities. Other computational methods for predicting the growth of instabilities are specifically designed to target one or more of these mechanisms, but are usually not general enough to capture them all. The complicated flowfields associated with realistic re-entry systems can excite all of these instability mechanisms as well as others that have not yet been identified. The simulation method proposed in this project is well suited for this scenario, since the optimization algorithm is able to account for all of these mechanisms. Much of the work needed to make this capability a reality lies in the details of the optimization algorithm. Several procedures for solving the optimization problem have been proposed [1, 11, 19], but the relative merits and drawbacks of these methods have not been analyzed. Likewise, there are many choices for the precise specification of the objective function used in the optimization, and the options used previously by other researchers are not believed to be suitable for transition prediction. The approach that will be taken in this project is to first apply the optimization algorithm to a simple, well-understood model problem, which will enable the numerical properties of different modeling choices to be assessed. The best practices determined by this exercise will then be incorporated in the full transition model.

To begin the process of validation of the new approach to transition prediction, comparisons will be made with wind tunnel data sets from the open literature and from tests previously conducted by Sandia. The data sets will include both sharp and blunted cones at zero degrees angles of attack.

1.2.2. Overview of the method

The core procedure used to predict the transition location in this project is an optimization method which determines the largest-growing disturbances that can develop in a laminar boundary layer. In this section, a high-level overview is given of the mathematical foundation behind the method without giving any specifics of the actual implementation.

The core optimization procedure used to predict transition can be constructed in one of two ways. In the first framework, known as the *temporal method*, the optimization problem is treated as an initial-value problem in which the most dangerous initial condition is sought. The amplification of the initial condition over time is evaluated and the initial condition that grows the most over a specified time interval $t \in [0, t_{max}]$ is sought. Of course, the amplification achieved depends on the value of t_{max} that is chosen, so optimizations must be conducted for multiple values of t_{max} in order to find the worst-case initial condition. The temporal method can be inefficient for convective instabilities, which amplify as they propagate downstream, but is very useful for analyzing absolute instabilities which remain constrained to a specific region of the flow (such as instabilities in a separation bubble).

The second framework for applying the optimization procedure is known as the *spatial method*. In this method, time-periodic disturbances having a fixed, real frequency are analyzed. The disturbances are assumed to originate at the boundaries of the domain (typically the inflow boundary) and the optimization procedure is used to determine the inflow disturbance type that achieves the largest growth as it interacts with the boundary layer. Since this analysis considers only one frequency at a time, multiple analyses must be carried out to analyze each possible frequency and determine the most dangerous disturbance selected from among all frequencies. The spatial method tends to be more efficient than the temporal method for analyzing convective instabilities, such as those typically encountered in planar boundary layers. Additionally, since disturbance sources in wind tunnels are typically characterized using frequency dependent power spectra, the spatial method has an advantage of being easy to compare with experimental data.

In the following sections, the mathematical details of the spatial and temporal methods are described. As will be seen, the two methods can be cast in very similar mathematical forms so that the same high-level procedure can be used for both methods.

1.2.2.1. Temporal Method

Consider a state vector $\mathbf{q}(x, y, z, t)$ which contains as its components the fluctuations in velocity and thermodynamic quantities. The linearized Navier-Stokes equations in this situation have the form:

$$\frac{\partial \mathbf{q}}{\partial t} = \mathcal{L}\mathbf{q} \tag{1.1}$$

where $\mathcal{L}$ is the operator that represents the linearized dynamics of the Navier-Stokes equations. If the state vector has initial components $\mathbf{q}_o$ at time $t = 0$, then the fluctuations evolve according to

exponential of the operator (or matrix) describing the linear dynamics:

$$\mathbf{q} = e^{\mathcal{L}t}\mathbf{q}_o \tag{1.2}$$

In order to maximize the disturbance, it is necessary to define a measure of its magnitude. Leaving the precise specification undetermined for now, the energy E of the disturbance is defined by a suitable inner product:

$$E = (\mathbf{q}, \mathbf{q}) \tag{1.3}$$

For a given linear operator $\mathcal{L}$, this inner product implies an adjoint operator $\mathcal{L}^+$ which satisfies the following relation for two arbitrary vector fields $\mathbf{u}$ and $\mathbf{v}$:

$$(\mathcal{L}\mathbf{u}, \mathbf{v}) = (\mathbf{u}, \mathcal{L}^+\mathbf{v}) \tag{1.4}$$

Using the foregoing results, the increase in energy of the disturbance from time $t = 0$ to the maximum time $t = \tau$ is given by:

$$\frac{E(\tau)}{E_o} = \frac{(e^{\mathcal{L}\tau}\mathbf{q}_o, e^{\mathcal{L}\tau}\mathbf{q}_o)}{(\mathbf{q}_o, \mathbf{q}_o)} = \frac{(\mathbf{q}_o, e^{\mathcal{L}^+\tau}e^{\mathcal{L}\tau}\mathbf{q}_o)}{(\mathbf{q}_o, \mathbf{q}_o)} \tag{1.5}$$

This form is recognized as a Rayleigh quotient; the ratio $E(\tau)/E_o$ is an eigenvalue of the combined linear operator $e^{\mathcal{L}^+\tau}e^{\mathcal{L}\tau}$ and the initial condition $\mathbf{q}_o$ is a right eigenvector. The "optimal" initial condition is the right eigenvector belonging to the eigenvalue that acheives the highest disturbance energy. A well-established method for solving eigenvalue problems of this type is the power iteration method, in which an initial guess of $\mathbf{q}_o$ is repeatedly multiplied by the combined operator $e^{\mathcal{L}^+\tau}e^{\mathcal{L}\tau}$ until convergence is reached. This procedure converges rapidly when the eigenvalues are well separated; if this is not the case, Krylov methods which involve multiple eigenvalues and eigenvectors can be used.

As described above, the optimization method is reduced to repeatedly multiplying the initial condition $\mathbf{q}_o$ against the combined linear operator $e^{\mathcal{L}^+\tau}e^{\mathcal{L}\tau}$. The action of the forward operator $e^{\mathcal{L}\tau}$ can be approximated by discretizing Equation 1.1 and integrating forward in time from $t = 0$ to $t = \tau$ using any suitable explicit or implicit numerical method. This can be carried out using a standard CFD code by either linearizing the code or simulating disturbances small enough to remain in the linear regime.

Similarly, the adjoint operator $e^{\mathcal{L}^+\tau}$ is the solution of the adjoint partial differential equation

$$\frac{\partial \mathbf{q}}{\partial t} + \mathcal{L}^+\mathbf{q} = 0 \tag{1.6}$$

The action of this equation can be approximated by discretizing Equation 1.6 and integrating backward in time from $t = \tau$ to $t = 0$ using any suitable numerical method. The "initial condition" at $t = \tau$ for this marching procedure is the product $e^{\mathcal{L}\tau}\mathbf{q}_o$ determined above. The final result at $t = 0$ is then a discrete approximation to the operation $e^{\mathcal{L}^+\tau}e^{\mathcal{L}\tau}\mathbf{q}_o$. Thus, repeated application of the direct and adjoint time marching procedures has the effect of performing power iterations on the composite operator $e^{\mathcal{L}^+\tau}e^{\mathcal{L}\tau}$. Using the above procedure, the temporal optimization problem can be solved using any CFD code provided that the code can solve the linearized equations and their adjoint counterparts.

1.2.2.2. Spatial Method

The spatial method can be constructed in a manner analogous to the temporal method above. Following a Laplace transform with respect to time, the linearized Navier-Stokes equations take the form:

$$(F - i\omega\mathbb{I})\mathbf{q} = B\mathbf{f} \tag{1.7}$$

where ω is the frequency, $\mathbb{I}$ is the identity operator, and F is the flux term of the Navier-Stokes equation. The operator B maps the external forcing $\mathbf{f}$ onto the solution variables $\mathbf{q}$ at the boundaries of the domain and is zero on the interior of the domain.

The second framework for constructing the optimization problem is known as the *spatial method*. In this approach, a periodic forcing with frequency ω is applied either at the boundary or the interior of the simulation domain. Such a problem can be cast in the form:

$$\mathcal{L}\mathbf{q} = B\mathbf{f} \tag{1.8}$$

where $\mathbf{f}(\omega)$ is a periodic forcing function that represents either volumetric forcing or the action of non-homogeneous boundary conditions. Defining the resolvent operator by $\mathbf{q} = \mathcal{R}\mathbf{f}$, the normalized energy of the fluctuations is given by

$$\frac{E(\omega)}{E_f} = \frac{(\mathcal{R}\mathbf{f}, \mathcal{R}\mathbf{f})}{(\mathbf{f}, \mathbf{f})} = \frac{(\mathbf{f}, \mathcal{R}^{+}\mathcal{R}\mathbf{f})}{(\mathbf{f}, \mathbf{f})} \tag{1.9}$$

This again represents an eigenvalue problem, in which the most dangerous forcing is the right eigenvector of the operator $\mathcal{R}^{+}\mathcal{R}$ corresponding to the largest positive eigenvalue. In the same manner as the temporal problem, the spatial problem can be solved using the power iteration method.

The two methods described above both boil down to solving an eigenvalue problem using the power iteration method, which requires repeated application of the linear system operator and its adjoint. Determining whether one of these two methods is superior to the other is an objective of this research.

2. LINEARIZED NAVIER-STOKES EQUATIONS

At the core of the optimization procedure used in this project lies the solution of the direct and adjoint linearized Navier-Stokes equations. These equations describe the amplification and evolution of small disturbances within the laminar boundary layer, which are believed to be the cause of transition to turbulence in low-disturbance environments. This chapter describes these equations and the methods used to solve them.

2.1. Equations of Motion

For a calorically perfect, non-reacting compressible gas, the fully nonlinear equations of continuity, momentum, energy, and state can be expressed in the following form:

$$\frac{\partial \rho}{\partial t} + \nabla \cdot (\rho \mathbf{u}) = 0 \tag{2.1a}$$

$$\rho \left(\frac{\partial \mathbf{u}}{\partial t} + \mathbf{u} \cdot \nabla \mathbf{u} \right) + \nabla p = \nabla \cdot \tau \tag{2.1b}$$

$$\rho C_v \left(\frac{\partial T}{\partial t} + \mathbf{u} \cdot \nabla T \right) + \rho R T \nabla \cdot \mathbf{u} = \nabla \cdot \mathbf{q} + \Phi \tag{2.1c}$$

$$p = \rho R T \tag{2.1d}$$

Here ρ is the fluid density, p the pressure, T the temperature, and $\mathbf{u}$ the velocity vector with Cartesian components (u, v, w). The specific heat at constant volume is denoted C_v, the gas constant is R, and the viscous stress tensor is denoted τ with components

$$\tau_{ij} = \mu \left(\frac{\partial u_i}{\partial x_j} + \frac{\partial u_j}{\partial x_i} \right) + \lambda \frac{\partial u_k}{\partial x_k} \tag{2.2}$$

where μ is the shear viscosity, λ the second viscosity, and Einstein summation notation is used on the vector indices. The heat flux vector $\mathbf{q}$ has components

$$q_i = -k \frac{\partial T}{\partial x_i} \tag{2.3}$$

where k is the thermal conductivity. The viscous dissipation per unit volume, Φ, is given by the contraction of the velocity gradient tensor against the shear stress tensor:

$$\Phi = \tau_{ij}\frac{\partial u_i}{\partial x_j} \tag{2.4}$$

In this project, the analysis is restricted to flows of a calorically perfect ideal gas. However, application of this method to flight cases may require that the addition of physics associated with chemical reactions and thermo-chemical non-equilibrium.

2.1.1. Linearized Equations

The equations of motion (2.2) can be linearized to produce the linearized Navier-Stokes equations:

$$\frac{\partial \tilde{\rho}}{\partial t} + \nabla\cdot(\bar{\mathbf{u}}\tilde{\rho} + \bar{\rho}\tilde{\mathbf{u}}) = 0 \tag{2.5}$$

$$\bar{\rho}\left(\frac{\partial \tilde{\mathbf{u}}}{\partial t} + \bar{\mathbf{u}}\cdot\nabla\tilde{\mathbf{u}} + \tilde{\mathbf{u}}\cdot\nabla\bar{\mathbf{u}}\right) + \tilde{\rho}\bar{\mathbf{u}}\cdot\nabla\bar{\mathbf{u}} + \nabla\tilde{p} = \nabla\cdot\tilde{\tau} \tag{2.6}$$

$$\bar{\rho}C_v\left(\frac{\partial \tilde{T}}{\partial t} + \bar{\mathbf{u}}\cdot\nabla\tilde{T} + \tilde{\mathbf{u}}\cdot\nabla\bar{T}\right) + \tilde{\rho}C_v\bar{\mathbf{u}}\cdot\nabla\bar{T} + \tilde{p}\nabla\cdot\bar{\mathbf{u}} + \bar{p}\nabla\cdot\tilde{\mathbf{u}} = \nabla\cdot\tilde{\mathbf{q}} + \tilde{\Phi} \tag{2.7}$$

The components of the fluctuating viscous stress tensor, heat flux vector, and viscous dissipation are given by:

$$\tilde{\tau}_{ij} = \bar{\mu}\left(\frac{\partial \tilde{u}_i}{\partial x_j} + \frac{\partial \tilde{u}_j}{\partial x_i}\right) + \bar{\lambda}\frac{\partial \tilde{u}_k}{\partial x_k} + \tilde{\mu}\left(\frac{\partial \bar{u}_i}{\partial x_j} + \frac{\partial \bar{u}_j}{\partial x_i}\right) + \tilde{\lambda}\frac{\partial \bar{u}_k}{\partial x_k} \tag{2.8a}$$

$$\tilde{q}_i = \bar{k}\frac{\partial \tilde{T}}{\partial x_i} + \tilde{k}\frac{\partial \bar{T}}{\partial x_i} \tag{2.8b}$$

$$\tilde{\Phi} = \bar{\tau}_{ij}\frac{\partial \tilde{u}_i}{\partial x_j} + \tilde{\tau}_{ij}\frac{\partial \bar{u}_i}{\partial x_j} \tag{2.8c}$$

The linear fluctuations in transport properties are then written in terms of the temperature fluctuations:

$$\tilde{\mu} = \frac{\partial \mu}{\partial T}\tilde{T} \tag{2.9}$$

$$\tilde{k} = \frac{\partial k}{\partial T}\tilde{T} \tag{2.10}$$

$$\tilde{\lambda} = \frac{\partial \lambda}{\partial T}\tilde{T} \tag{2.11}$$

Using these definitions, the linearized Navier-Stokes equations in two dimensions can be written in the form of a first-order system as follows:

$$\mathbf{A}_t\frac{\partial \mathbf{Q}}{\partial t} + \mathbf{A}_x\frac{\partial \mathbf{Q}}{\partial x} + \mathbf{A}_y\frac{\partial \mathbf{Q}}{\partial y} = 0 \tag{2.12}$$

In this equation, $\mathbf{Q}$ is the vector of disturbances

$$\mathbf{Q} = \left(\tilde{\rho}, \tilde{u}, \tilde{v}, \tilde{T}, \tilde{\tau}_{xx}, \tilde{\tau}_{xy}, \tilde{\tau}_{yy}, \tilde{q}_x, \tilde{q}_y\right)^T \tag{2.13}$$

and $\mathbf{A}_t$, $\mathbf{A}_x$, and $\mathbf{A}_y$ are 9×9 matrices. This system can equivalently be written as a set of four second order partial differential equations by substituting the definitions of the viscous stress tensor and heat flux vector.

3. OPTIMIZATION PROBLEM

3.1. Introduction

In this chapter, the details of the optimization problem which determines the most amplified disturbances is described. Before considering the details associated with the Navier-Stokes equations, the generic principles of the optimization method are described.

Consider a time-varying dynamical system consisting of N states, where the ith state is denoted $q_i(t)$. The collection of all N states is represented by a column vector $\mathbf{q}(t)$ of length N containing the state values as its elements. Suppose further that the size of the disturbance is described by an arbitrary quadratic function of the state variables of the form:

$$E(T) = \mathbf{q}^T \mathbf{M} \mathbf{q} \tag{3.1}$$

Here E is the energy, or magnitude of the disturbance and M is a $N \times N$ matrix. The goal of the optimization problem is to find the initial conditions $\mathbf{q}_o = \mathbf{q}(t=0)$ that maximize the energy E at some time T. The initial conditions are subject to the constraint that the initial energy of the system has some prescribed value E_o. Using the Lagrange multiplier technique, this objective is met by maximizing the objective function:

$$J = \mathbf{q}^T \mathbf{M} \mathbf{q} - \lambda(\mathbf{q}_o^T \mathbf{M} \mathbf{q}_o - E_o) \tag{3.2}$$

where λ is a Lagrange multiplier. The state vector at time T can be expressed in terms of the resolvent operator $\mathcal{R}$, which maps the initial condition $\mathbf{q}_o$ onto the final result $\mathbf{q}(T)$:

$$\mathbf{q}(T) = \mathcal{R}(T)\mathbf{q}_o \tag{3.3}$$

With this result, the optimization problem becomes

$$J = \mathbf{q}_o^T \mathcal{R}^T \mathbf{M} \mathcal{R} \mathbf{q}_o - \lambda(\mathbf{q}_o^T \mathbf{M} \mathbf{q}_o - E_o) \tag{3.4}$$

This problem is solved by setting the partial derivatives with respect to each initial state varible, $q_{o,i}$ equal to zero, as well as setting the derivative with respect to λ equal to zero. These operations produce a system of $N+1$ equations:

$$\frac{\partial J}{\partial \mathbf{q}_o} = 0 = \mathbf{q}_o^T \left[\mathcal{R}^T \mathbf{M} \mathcal{R} - \lambda \mathbf{M}\right] \tag{3.5}$$

$$\frac{\partial J}{\partial \lambda} = 0 = \mathbf{q}_o^T \mathbf{M} \mathbf{q}_o - E_o \tag{3.6}$$

Equation 3.5 is an eigenvalue problem with eigenvalue λ and left eigenvector $\mathbf{q}_o^T$, while Equation 3.6 specifies the normalization of the eigenvector. For the special case in which $\mathbf{M} = \mathbb{I}$, the eigenvalue problem reduces to:

$$|\mathcal{R}^T \mathcal{R} - \lambda| = 0 \tag{3.7}$$

The optimization problem which determines the most amplified disturbances can be prescribed using one of two frameworks: the temporal and spatial frameworks. The temporal framework considers the temporal response of the linear system to an initial condition, while the spatial framework considers the response of the linear system to time-periodic forcing or time-periodic boundary conditions. One objective of this study is to determine which formulation is best suited for transition prediction. In the following sections, these two approaches are described in detail.

3.2. Temporal Analysis / Initial-Value Problem

In the temporal analysis, the linearized Navier-Stokes equations are cast as an initial-value problem of the following form:

$$\frac{\partial \mathbf{q}}{\partial t} + \mathcal{L}\mathbf{q} = 0 \tag{3.8}$$

$$\mathbf{q}(t=0) = \mathbf{q}_o \tag{3.9}$$

Here $\mathbf{q}$ is the vector of state variables, $\mathcal{L}$ is a linear operator representing the linearized Navier-Stokes equations, and $\mathbf{q}_o$ is the initial condition. The objective of the analysis is to determine the initial condition that produces the largest perturbation amplitude at some later time T. In order to accomplish this, a measure of the disturbance amplitude must be proposed. A general measure of the disturbance energy E takes the following form:

$$E(\mathbf{q})^2 = \mathbf{q}^H \mathbf{M} \mathbf{q} \tag{3.10}$$

where $\mathbf{M}$ is a matrix of weights and superscript H denotes the conjugate (Hermitian) transpose. By selecting a suitable weight matrix $\mathbf{M}$, this energy can be set equal to the kinetic energy, the sum of the kinetic, acoustic, and thermal energies, or a variety of other choices.

Having introduced the energy metric, the optimization problem involves the process of maximizing the energy at time T while constraining the energy at time $t = 0$. This can be achieved by minimizing the Lagrange functional [19]:

$$\mathbf{J} = \int_{\Omega_o} \langle \mathbf{q}(T), \mathbf{q}(T) \rangle dV - \int_0^T \int_\Omega \left\langle \mathbf{v}, \frac{\partial \mathbf{q}}{\partial t} + \mathcal{L}\mathbf{q} \right\rangle dV - \lambda \left(\int_{\Omega_i} \langle \mathbf{q}_o, \mathbf{q}_o \rangle dV - 1 \right) \tag{3.11}$$

For generality, three different volume domains are considered: Ω_o is the optimization volume, Ω_i is the input domain, and Ω is the full computational domain. Separate domains are considered because one might wish to allow initial disturbances only over some subset of the computational volume, or one might wish to maximize the resulting disturbance over a different subdomain. The first term in Equation 3.11 contains the disturbance energy integrated over the output domain. The second term is a penalty term that forces the disturbances to adhere to the linearized Navier-Stokes equations, using a vector of Lagrange multipliers $\mathbf{v}$ (also known as the adjoint solution vector or the co-state vector) to enforce this condition over the entire domain Ω. Finally, the last term enforces the initial disturbance energy to be 1.0 when integrated over the input domain Ω_i, and λ is the Lagrange multiplier corresponding to this constraint. Solving the

optimization problem then consists in minimizing the functional **J**, which is accomplished by setting the gradients of **J** with respect to each variable independently equal to zero.

Setting the first variation of **J** with respect to **v** equal to zero results in the following condition:

$$\frac{\partial \mathbf{q}}{\partial t} + \mathcal{L}\mathbf{q} = 0 \tag{3.12}$$

which recovers the linearized Navier-Stokes equations. Using integration by parts, the second term in Equation 3.11 can be written in the form:

$$\int_0^T \int_\Omega \left\langle \mathbf{v}, \frac{\partial \mathbf{q}}{\partial t} + \mathcal{L}\mathbf{q} \right\rangle dV = \int_0^T \int_\Omega \left\langle -\frac{\partial \mathbf{v}}{\partial t} - \mathcal{L}^+\mathbf{v}, \mathbf{q} \right\rangle dV + \int_\Omega \langle \mathbf{v}(T), \mathbf{q}(T) \rangle dV - \int_\Omega \langle \mathbf{v}(0), \mathbf{q}(0) \rangle dV + \text{B.T.} \tag{3.13}$$

where $\mathcal{L}^+$ is the adjoint linear operator and "B.T." stands for boundary terms, which are set to zero by selecting suitable boundary conditions on the adjoint solution **v**. Using Equation 3.13, setting the first variation of **J** with respect to **q** equal to zero results in the following condition:

$$-\frac{\partial \mathbf{v}}{\partial t} - \mathcal{L}^+\mathbf{v} = 0 \tag{3.14}$$

This equation defines the adjoint solution **v**. Finally, taking the first variation of J with respect to the initial and final states $\mathbf{q}(0)$ and $\mathbf{q}(T)$ results in the following conditions:

$$2\lambda \int_{\Omega_i} \mathbf{q}(0) dV = \int_\Omega \mathbf{v}(0) dV \tag{3.15}$$

$$2 \int_{\Omega_o} \mathbf{q}(T) dV = \int_\Omega \mathbf{v}(T) dV \tag{3.16}$$

The fact that the two sides of these equations are integrated over different volumes can be managed by introducing the functions δ_i and δ_o, which are equal to 1.0 inside Ω_i and Ω_o (respectively) and equal to zero elsewhere. The optimality conditions then read:

$$2\lambda \int_\Omega \mathbf{q}(0) \delta_i dV = \int_\Omega \mathbf{v}(0) dV \tag{3.17}$$

$$2 \int_\Omega \mathbf{q}(T) \delta_o dV = \int_\Omega \mathbf{v}(T) dV \tag{3.18}$$

The solutions to the direct and adjoint equations can be written in terms of the matrix exponential as:

$$\mathbf{q} = \mathbf{q}(0) e^{\mathcal{L}t} \tag{3.19}$$

$$\mathbf{v} = \mathbf{v}(T) e^{\mathcal{L}^+ t} \tag{3.20}$$

Combining all these results produces the following result:

$$\lambda \mathbf{q}(0) = e^{\mathcal{L}^+ T} e^{\mathcal{L}T} \mathbf{q}(0) \tag{3.21}$$

This equation can be viewed as an eigenvalue problem involving the matrix exponentials of the linear operator $\mathcal{L}$ and its adjoint. The most amplified disturbance corresponds to the largest eigenvalue λ of this system. The matrix exponentials can be numerically approximated by time-marching the direct and adjoint linearized Navier-Stokes equations. The direct-adjoint marching procedure is equivalent to performing power iterations on the eigenvalue problem above. Sub-optimal disturbances can be found using Krylov sub-space iteration to approximate the eigenvalues.

3.3. Spatial Analysis / Boundary-Value Problem

In the spatial analysis, the linearized Navier-Stokes equations are cast as a boundary-value problem of the following form:

$$-i\omega\mathbb{I}\mathbf{q} + \mathcal{L}\mathbf{q} = B\mathbf{f} \tag{3.22}$$

$$\mathbf{q}(x_{in}) = \mathbf{f} \tag{3.23}$$

where $\mathbf{f}$ denotes a time-periodic boundary condition and B is forcing function coefficient matrix.

The Lagrange functional is very similar to the temporal case (Equation 3.11) except that a boundary condition is used rather than an initial condition:

$$\mathbf{J} = \int_{\Omega_o} \langle \mathbf{q}, \mathbf{q} \rangle dV - \int_{\Omega} \langle \mathbf{v}, -i\omega\mathbb{I}\mathbf{q} + \mathcal{L}\mathbf{q} - B\mathbf{f} \rangle \, dV - \lambda \left(\int_{\partial\Omega_i} \langle \mathbf{f}, \mathbf{f} \rangle dA - 1 \right) \tag{3.24}$$

Here $\partial\Omega_i$ represents the inflow surface area.

Just as in the temporal case, setting to zero the first variations of $\mathbf{J}$ with respect to $\mathbf{v}$ produces the linearized Navier-Stokes equations:

$$\mathcal{L}\mathbf{q} - i\omega\mathbb{I}\mathbf{q} = B\mathbf{f} \tag{3.25}$$

To compute the variation with respect to the other variables, the relationship provided by integration by parts is used to replace the second term in Equation 3.24, which can be written in the form:

$$\int_{\Omega} \langle \mathbf{v}, -i\omega\mathbb{I}\mathbf{q} + \mathcal{L}\mathbf{q} \rangle = \int_{\Omega} \left\langle \mathcal{L}^{+}\mathbf{v} + i\omega\mathbb{I}\mathbf{v}, \mathbf{q} \right\rangle - \int_{\partial\Omega_i} \langle \mathbf{v}, \mathbf{f} \rangle \tag{3.26}$$

where $\mathcal{L}^{+}$ is again the adjoint linear operator and the last terms are the boundary terms. Setting the variation of $\mathbf{J}$ with respect to $\mathbf{q}$ generates the condition of the adjoint equation

$$\mathcal{L}^{+}\mathbf{v} + i\omega\mathbb{I}\mathbf{v} = 2\mathbf{q}$$

Setting the variation of $\mathbf{J}$ equal to zero with respect to the boundary value of $\mathbf{f}$ results in the following conditions:

$$2\lambda\mathbf{f} = \mathbf{v} \tag{3.27}$$

The last variation of $\mathbf{J}$ with respect to λ recovers the normalization condition

$$\int_{\partial\Omega_i} \langle \mathbf{f}, \mathbf{f} \rangle dA = 1.$$

3.4. Numerical Adjoints

Following discretization, the linearized Navier-Stokes equations can be represented as a large linear system of the semi-discrete form:

$$\frac{\partial \mathbf{q}}{\partial t} = \mathbf{A}\mathbf{q} \tag{3.28}$$

With the addition of explicit or implicit time discretization, the system takes the form:

$$\mathbf{B}\mathbf{q}^{n+1} = \mathbf{C}\mathbf{q}^{n} \tag{3.29}$$

where the superscript n represents the time level. Some examples of values for the $\mathbf{B}$ and $\mathbf{C}$ matrices for different time discretizations are the following:

$$\text{Explicit Euler:} \qquad \mathbf{B} = \mathbb{I} \qquad \mathbf{C} = (\mathbb{I} + \mathbf{A}\Delta t) \tag{3.30}$$

$$\text{Implicit Euler:} \qquad \mathbf{B} = \mathbb{I} - \mathbf{A}\Delta t \qquad \mathbf{C} = \mathbb{I} \tag{3.31}$$

Similar expressions can be written for other higher-order discretization schemes. For a given time discretization scheme, the term in the Lagrange functional corresponding to the linearized Navier-Stokes equations takes the form:

$$T \equiv \int_0^T \mathbf{v}^H \left(\frac{\partial \mathbf{q}}{\partial t} - \mathbf{A}\mathbf{q} \right) dt \tag{3.32}$$

where $\mathbf{v}$ is the adjoint function and superscript H denotes the Hermitian transpose. Application of the time discretization leads to the following result:

$$T \approx \sum_{n=1}^{N} \mathbf{v}^n \left(\mathbf{B}\mathbf{q}^{n+1} - \mathbf{C}\mathbf{q}^{n} \right) \tag{3.33}$$

$$= \sum_{n=1}^{N} \left[\mathbf{v}^n \mathbf{B}\mathbf{q}^{n+1} + \mathbf{v}^{n+1}\mathbf{C}\mathbf{q}^{n+1} - \mathbf{v}^{n+1}\mathbf{C}\mathbf{q}^{n+1} - \mathbf{v}^n \mathbf{C}\mathbf{q}^{n} \right] \tag{3.34}$$

$$= \sum_{n=1}^{N} \left(\mathbf{v}^n \mathbf{B} - \mathbf{v}^{n+1}\mathbf{C} \right) \mathbf{q}^{n+1} + \left(\mathbf{v}^{n+1}\mathbf{C}\mathbf{q}^{n+1} - \mathbf{v}^N \mathbf{C}\mathbf{q}^{n} \right) \tag{3.35}$$

$$= \sum_{n=1}^{N} \left(\mathbf{v}^n \mathbf{B} - \mathbf{v}^{n+1}\mathbf{C} \right) \mathbf{q}^{n+1} + \mathbf{v}^N \mathbf{C}\mathbf{q}^{N} - \mathbf{v}^1 \mathbf{C}\mathbf{q}^{1} \tag{3.36}$$

This result is the discrete analogue of integration by parts, producing a discrete system of equations for the adjoint along with boundary terms. For first order explicit and implicit time discretizations, the adjoint system can be written:

$$\text{Explicit Euler:} \qquad \mathbf{v}^n \mathbb{I} = \mathbf{v}^{n+1} \left(\mathbb{I} + \mathbf{A}\Delta t \right) \tag{3.37}$$

$$\text{Implicit Euler:} \qquad \mathbf{v}^n \left(\mathbb{I} - \mathbf{A}\Delta t \right) = \mathbf{v}^{n+1} \mathbb{I} \tag{3.38}$$

These can be re-cast as:

$$-\frac{\mathbf{v}^{n+1} - \mathbf{v}^n}{\Delta t} = \mathbf{A}\mathbf{v}^{n+1} \tag{3.39}$$

$$-\frac{\mathbf{v}^{n+1} - \mathbf{v}^n}{\Delta t} = \mathbf{A}\mathbf{v}^{n} \tag{3.40}$$

These can be viewed as explicit and implicit integration in the negative time direction.

3.5. Finite Volume Formulation

The nonlinear equations of compressible fluid mechanics can be represented in conservation form as:

$$\frac{\partial \mathbf{U}}{\partial t} + \mathbf{R} = 0 \tag{3.41}$$

where $\mathbf{U}$ is the vector of conserved variables and $\mathbf{R}$ is the residual vector composed of the inviscid and viscous flux terms. In the steady base flow calculation, the residual vector $\mathbf{R}$ is driven to zero.

The unsteady, linearized equations of motion are then written as:

$$\frac{\partial \tilde{U}_i}{\partial t} + \sum_j \frac{\partial R_i}{\partial U_j}\tilde{U}_j + \sum_k \frac{\partial R_i}{\partial G_k}\tilde{G}_k = 0 \tag{3.42}$$

Here $\tilde{U}_i$ is an element of the perturbed state vector, $\partial R_i/\partial U_j$ is the sensitivity of the residual at cell i to perturbations in the solution at cell j, and $\partial R_i/\partial G_k$ is the sensitivity of the residual to perturbations in the k^{th} ghost cell. The values $\tilde{G}_k$ are the perturbation boundary conditions.

In the spatial problem, we seek to determine the perturbation boundary conditions G_k that maximize the energy of the disturbance $\tilde{\mathbf{U}}$. This optimization problem is expressed in terms of the objective function $\mathcal{J}$:

$$\mathcal{J} = \sum_i \tilde{U}_i^* W_i \tilde{U}_i - \sum_i V_i^* \left[-\mathbb{I}\omega\tilde{U}_i + \sum_j \frac{\partial R_i}{\partial U_j}\tilde{U}_j + \sum_k \frac{\partial R_i}{\partial G_k}\tilde{G}_k \right] - \lambda \left(\sum_k \tilde{G}_k^* W_k \tilde{G}_k - E_o \right) \tag{3.43}$$

The first term is the energy of the disturbance, which is computed as an inner product of the solution variables $\tilde{U}_i$ against the weights W_i. The second term is the linearized Navier-Stokes equations from Equation 3.42, multiplied by the Lagrange multipliers V_i, which can also be interpreted as adjoint variables. The third term is a constraint that the energy of the boundary values $\tilde{G}_k$, integrated against the weights W_k, must be equal to a specified value E_o (usually taken to be 1.0). This term is multiplied by a Lagrange multiplier λ.

To maximize the objective function $\mathcal{J}$, the derivative with respect to each unknown is set to zero. Taking the derivative with respect to the adjoint variables V_i yields Equation 3.42:

$$\frac{\partial \mathcal{J}}{\partial V_i} = 0 = -\mathbb{I}\omega\tilde{U}_i + \sum_j \frac{\partial R_i}{\partial U_j}\tilde{U}_j + \sum_k \frac{\partial R_i}{\partial G_k}\tilde{G}_k \tag{3.44}$$

Taking the derivative with respect to the state variables $\tilde{U}_p$ yields the condition:

$$\frac{\partial \mathcal{J}}{\partial U_p} = 0 = 2\tilde{U}_p^* W_p - \sum_i V_i^* \left[-i\omega\delta_{ip} + \frac{\partial R_i}{\partial U_p} \right] \tag{3.45}$$

where δ_{ip} i the Kronecker delta. This equation can be transposed to form the adjoint equations of motion:

$$\frac{\partial R_i}{\partial U_p}\tilde{V}_i - i\omega\tilde{V}_p = 2W_p\tilde{U}_p \tag{3.46}$$

Taking the derivative of $\mathcal{J}$ with respect to the ghost cells leads to the optimization condition:

$$\frac{\partial \mathcal{J}}{\partial G_k} = 0 = \sum_i V_i^* \frac{\partial R_i}{\partial G_k} + 2\lambda G_k^* W_k \tag{3.47}$$

which is rearranged to form:

$$G_k = -\frac{1}{2\lambda W_k}\left(\sum_i V_i^* \frac{\partial R_i}{\partial G_k}\right)^* \tag{3.48}$$

The final criterion is to minimize $\mathcal{J}$ with respect to the Lagrange multiplier λ:

$$\frac{\partial J}{\partial \lambda} = 0 = \sum_k \tilde{G}_k^* W_k \tilde{G}_k - E_o \tag{3.49}$$

This is merely a normalization condition on the boundary values $\tilde{G}_k$.

3.6. Implementation details

To generate the Jacobian matrices $\frac{\partial R}{\partial U}$ and $\frac{\partial R}{\partial G}$, an automatic differentiation approach is used. The floating point data type in the SPARC CFD code is replaced by an automatic differentiation data type as implemented in the Sacado package of the Trilinos software suite [20]. This data type supplies an overloaded implementation for each standard numerical operation, and the overloaded operator applies the chain rule of differentiation to each successive operation to track the overall derivative of a function call with exact numerical precision. This technique is used to compute the derivative of the residual (**R** in Equation 3.41) with respect to the state variables in the interior cells U and ghost cells G. Furthermore, the Jacobian "coloring" technique is used to reduce the computation expense of the Jacobian matrix calculation [9]. With this method, the sparsity of the Jacobian matrix is exploited to compute multiple rows of the Jacobian matrix using a single evaluation of the residual.

The automatic differentiation (AD) data type is also used to store both the mean-flow solution and the perturbation quantities. For the temporal approach there is only one linearized perturbation quantity. For the spatial approach we use two perturbation quantities to separately store the real and imaginary parts of the complex-valued perturbation. Calculations performed using the AD data type then produce an AD-valued result with both mean and linearized perturbation components. This allows us to compute the linearized perturbation component of the the flux residual **R** without modifying any of the flux routines within SPARC.

Both the temporal and spatial analyses have been implemented in SPARC. The temporal analysis uses a standard BDF time integration scheme to solve for the resulting linearized flow solution when a perturbed initial condition is specified. The spatial analysis solves directly for the periodic steady state flow solution when periodic forcing is applied at the boundaries. Solving the spatial analysis problem would typically involve solving a complex-valued linear system. We avoid this by representing the complex-valued system by an equivalent real-valued system [8].

4. MODEL DEMONSTRATION AND VERIFICATION

4.1. Optimization Solver

In this section we overview how the optimization solver is used for flat plate boundary layer problems. This is a demonstration of the capabilities developed during the course of this project. For simplicity, we are looking only at the initial value problem rather than the spatial problem. Application of the spatial problem will be shown in the next section for sharp and blunt cone geometries, sections 5.3 and 5.4 respectively.

4.1.1. Optimization Algorithm Demonstration

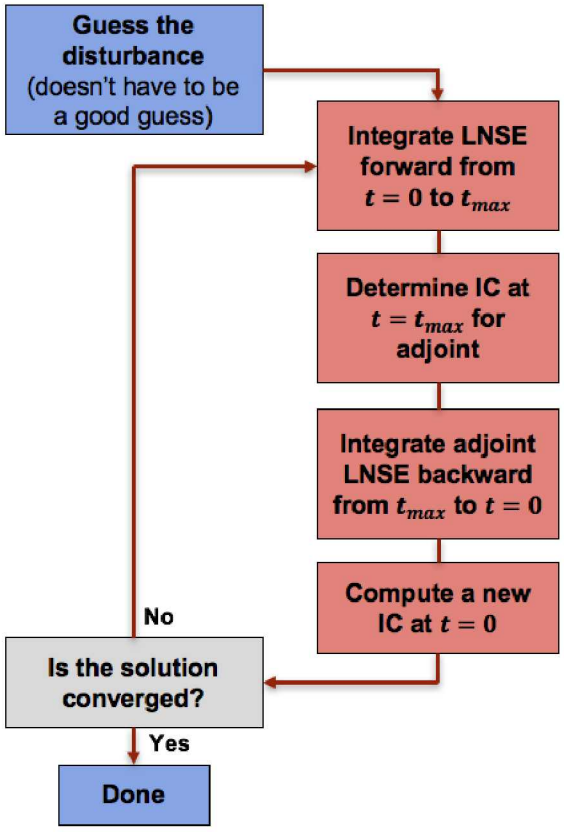

Figure 4-1. Flow chart of the optimization loop.

A flow chart of the optimization loop is shown in Figure 4-1. The first step is to make an initial guess. The initial guess does not have to be good, and can often just be random noise. The next step is to solve the direct (or forward) linearized Navier-Stokes problem for this given disturbance, integrating forward in time until the end of the simulation. Then, the appropriate mapping of the final forward solution to the adjoint initial solution is made, and the adjoint problem is solved integrating back in time. The final adjoint solution (at $t = 0$) is then appropriately mapped to the initial condition of the next forward solution, and the loop continues until the energy growth in the domain converges to a steady solution, as shown in Figure 4-2. In this case, the solution converges in about 5 iterations.

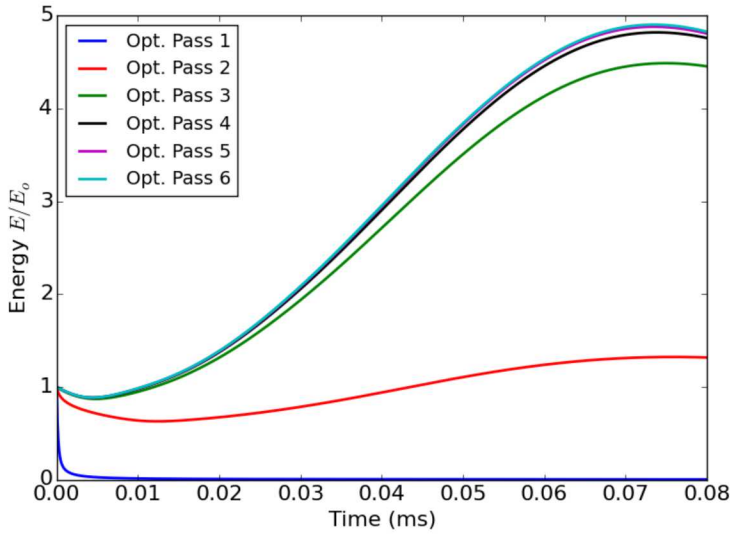

Figure 4-2. Energy growth (normalized by the initial energy) as a function of time. Each line represents a different optimization iteration.

A more detailed example of the optimization steps outlined earlier are displayed in Figure 4-3. In this case, we are considering a Mach 6 flow past a flat plate which is an adiabatic wall. The Reynolds number along the plate length spans from $Re = 3 \times 10^6 \rightarrow 17 \times 10^6$. The random noise initial condition is shown in Figure 4-3(a), and the final solution after the first optimization step is shown in Figure 4-3(b). Here, we can start to see the emergence of the most dangerous wave form leading to the maximal energy growth in this particular case. The first adjoint solve in the first optimization loop is shown in Figures 4-3(c-d). Here, the initial condition is mapped from the last iteration in the direct solve shown in Figure 4-3(b). The adjoint equation is stepped backwards in time until we arrive back at $t = 0$ in Figure 4-3(d). Skipping ahead, the final solution of the direct solve in the last optimization loop is shown Figures 4-3(e-f). The most dangerous initial wave packet is shown in Figure 4-3(e), which shows a cluster of waves on the boundary layer edge. This then perturbs the boundary layer and the most dangerous, highest energy growing disturbance is highlighted in Figure 4-3(f). This is a "2nd mode" transition mechanism common in these types of flat plate hypersonic flows. What's important here is that the optimization method was able to identify the initial condition (or wave packet) that is responsible for this growth.

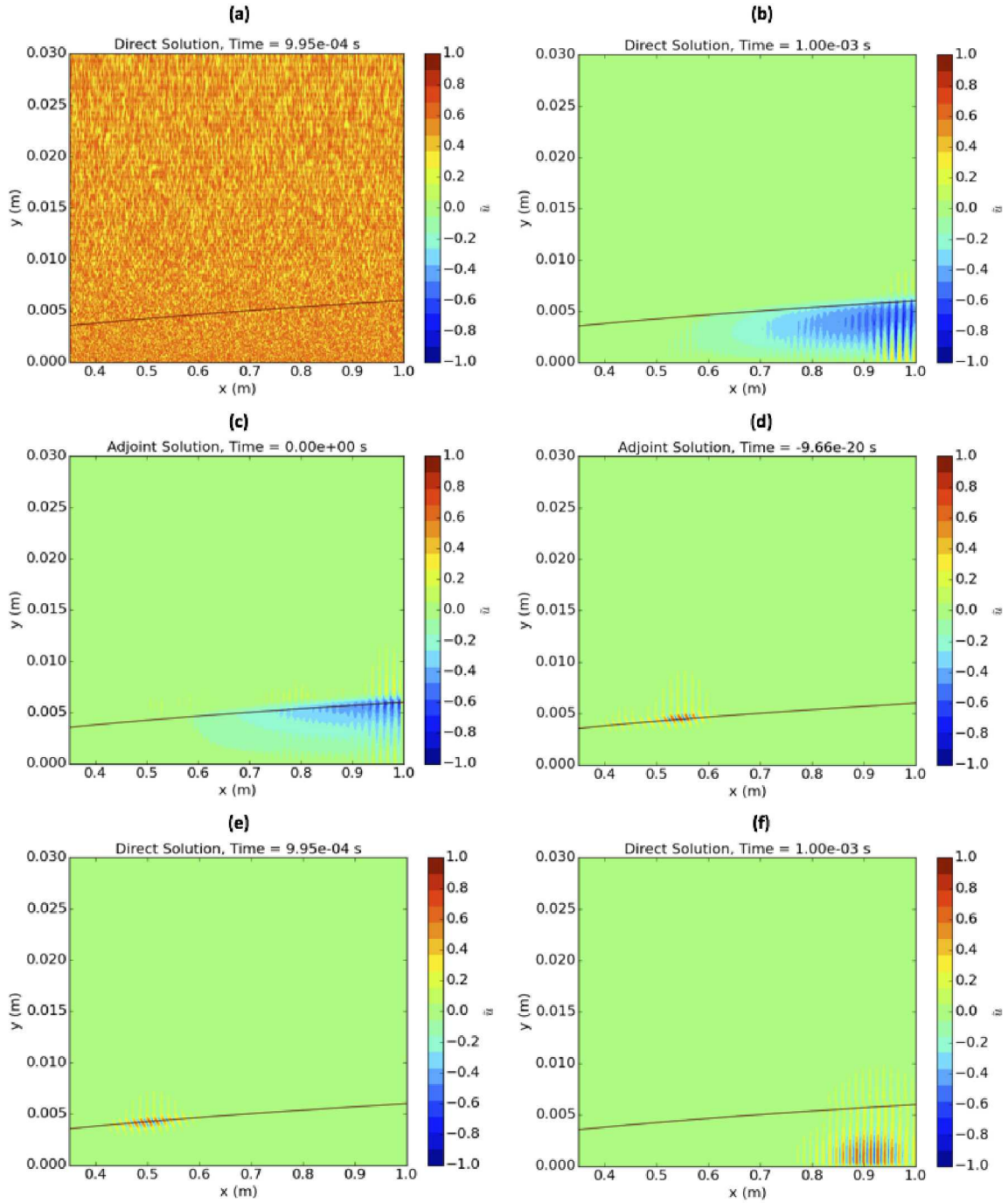

Figure 4-3. Example optimization problem for a Mach 6 flow past a flat plate with an adiabatic wall. $Re = 3 \times 10^6 \rightarrow 17 \times 10^6$**. (a) Initial condition in the first opt. step for the direct solution (random noise). (b) Final direct solution for the first op. step. (c) Initial condition of the adjoint variables in the first opt. step. (d) Final adjoint solution for the first opt. step. (e) Initial condition for the direct solution at the last opt. step. (f) Final direct solution for the last opt. step. Contours colored by streamwise disturbance velocity** u'

4.1.2. Constrained and Unconstrained Optimization

The previous section demonstrated the results of an unconstrained optimization problem. By unconstrained, we mean that both the initial condition and the objective function were allowed to be evaluated anywhere in the domain (inside or outside the boundary layer). For the case described above (and shown again in Figure 4-4), the optimized initial disturbance was located on the boundary layer edge, and the most amplified disturbance arising from this initial disturbance was found to grow in the boundary layer near the end of the solution domain. Unconstrained optimization works well, but it is rather trivial to add constraints to the optimization problem, the most straightforward constraint is to limit where the initial condition and objective function are evaluated in the domain. This allows us to fine-tune the optimization to exact areas of interest in our given problem.

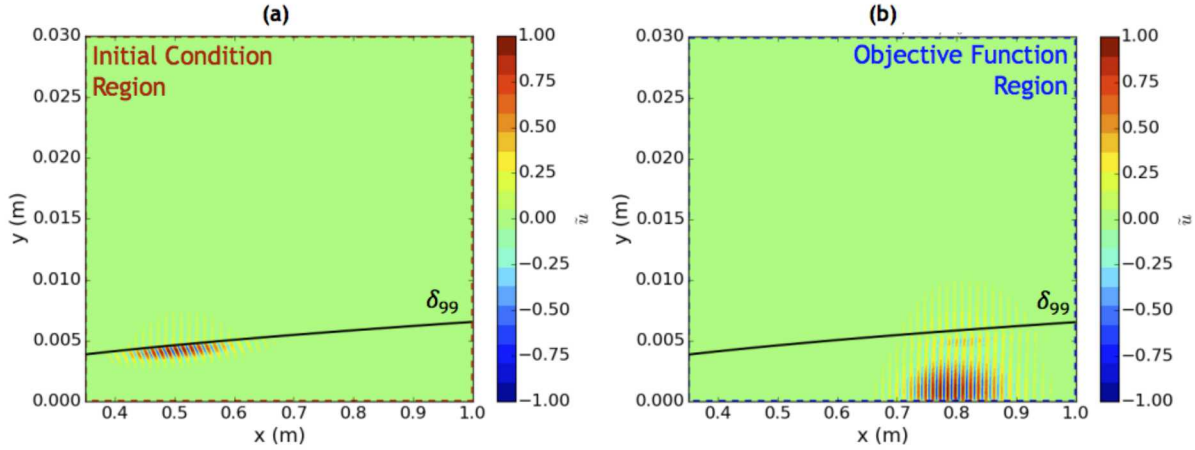

Figure 4-4. Example of an unconstrained optimization problem where the initial condition and objective function are unconstrained. (a) Optimized initial condition. (b) Optimized final disturbance. Contours are colored by the streamwise disturbance velocity u'

An example of a constrained optimization problem where the initial condition is constrained, but the objective function evaluation domain remains unconstrained is shown in Figure 4-5. The optimized energy was approximately 83% of the unconstrained optimization problem in Figure 4-4, but allows us to enforce that the initial condition comes from some specified region (outline in black in Figure 4-5(a). We do not place any restrictions on the objective function evaluation, and the most amplified disturbance again grows in the boundary layer (although further downstream than in the unconstrained case), shown in Figure 4-5(b).

An example of a constrained optimization problem where the initial condition is unconstrained, but the objective function evaluation domain is now constrained is shown in Figure 4-6. Here, the final optimized energy was approximately 93% of the unconstrained problem. The ability to fine tune where the objective function is evaluated can be quite powerful, as it can potentially allow you to "tune out" or "turn off" turbulent regions of the flow that you do not care to evaluate the objective function (in this case fluctuation energy).

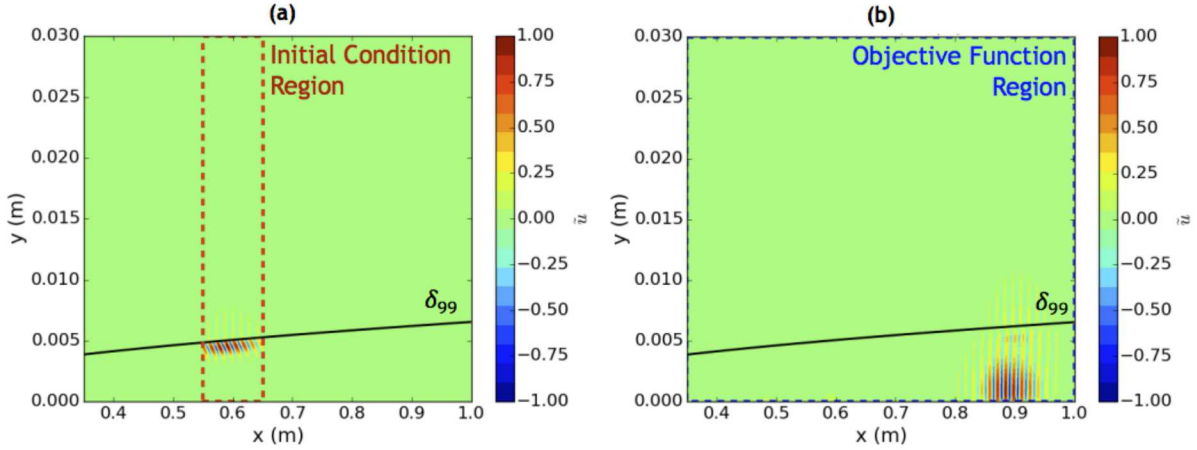

Figure 4-5. Example of an constrained optimization problem where the initial condition is constrained but the objective function is unconstrained. (a) Optimized initial condition. (b) Optimized final disturbance. Contours are colored by the streamwise disturbance velocity u'

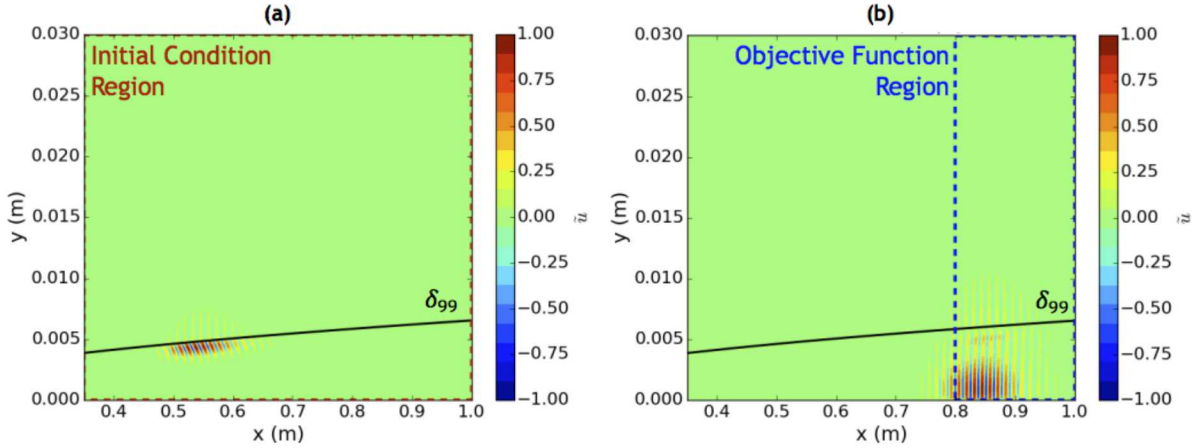

Figure 4-6. Example of an constrained optimization problem where the initial condition is unconstrained but the objective function is constrained. (a) Optimized initial condition. (b) Optimized final disturbance. Contours are colored by the streamwise disturbance velocity u'

Figure 4-7 shows a case where the initial condition is constrained only to exist in the freestream (e.g. outside of the boundary layer). This is an important distinction from the example shown in Figure 4-5, where only the streamwise location of the initial disturbance was constrained. The initial disturbance generated from that constraint still originated from the edge and within the boundary layer. However, if we want to consider a "receptivity" problem, we want to constrain the initial condition to exist outside of the boundary layer. In this case (Figure 4-7(a)), we can see that the initial disturbance resides outside of the boundary layer and is actually a 2nd mode wave (an acoustic wave) that travels parallel to the boundary layer edge. While the disturbance energy growth is only about 19% of the unconstrained optimization problem (receptivity is inefficient in this case), it is essential to predict transition in this fashion as receptivity may be the *only* way to

introduce disturbances in the boundary layer (usually through freestream forcing).

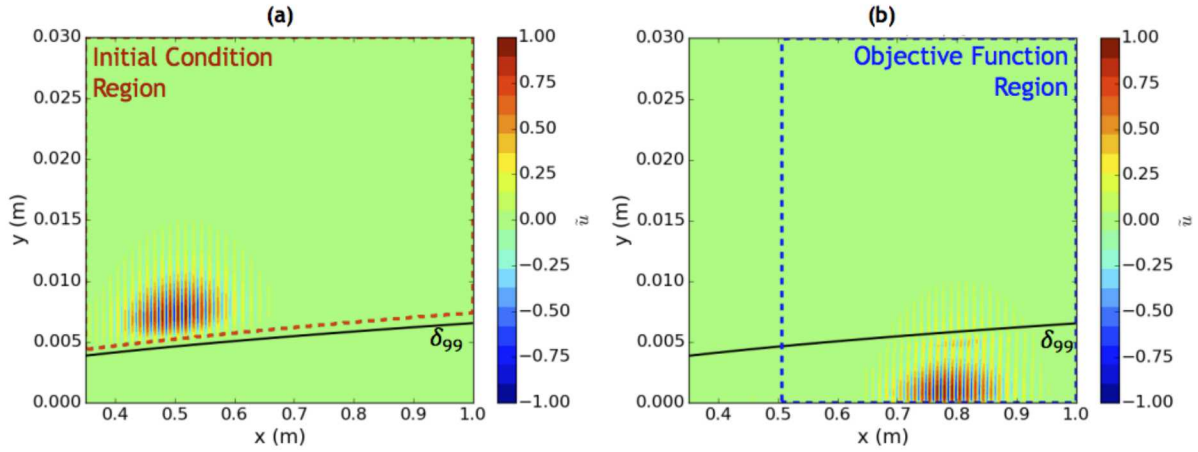

Figure 4-7. Example of a receptivity optimization problem where initial disturbances are constrained to lie outside of the boundary layer. (a) Optimized initial condition. (b) Optimized final disturbance. Contours are colored by the streamwise disturbance velocity u'

5. MODEL VALIDATION

In this chapter we validate the optimization method using numerous test problems of increasing complexity. Where available, details regarding the nature of the disturbance (such as frequency, wavelength, transition pattern) are compared with the predictions of the method. In other cases, particularly for flight comparisons, only transition locations are available for comparison with the optimization method.

5.1. Simulation Conditions

To test and demonstrate the transition prediction method, several experiments involving flow over a sharp or moderately blunt seven degree half-angle cone at zero angle of attack are selected. The simulation conditions are listed in Table 5-1. For each case, a two dimensional, axisymmetric grid was generated using approximately 12,000 streamwise points and 200 wall-normal points. Systematic grid convergence checks were performed for each case with both the laminar base flow and the linearized fluctuations recomputed for each grid refinement level. Convergence of the mesh was established by checking that the wall pressure magnitude differed by less than **2%** between meshes.

5.2. Base Flow Calculation

This paper attempts to predict laminar-turbulent transition on sharp cones at zero angle of attack. This calculation is attempted for two different wind tunnels: the AEDC Tunnel 9 facility operating at Mach 10 [15–17] and the Sandia National Laboratories Hypersonic Wind Tunnel (HWT) operating at Mach 8 [4]. In the Tunnel 9 facility, the test article is a 1.5 m long cone with a half-angle of 7° and a nose tip radius of 152 μm. In the HWT, the test article is a 0.5 m long 7° cone with a nose tip radius of 50 μm.

Table 5-1. Wind tunnel test conditions. M_∞ is the freestream Mach number, Re_∞ is the unit Reynolds number, and R_n is the nose radius.

Facility	M_∞	Re_∞ (1/m)	R_n (mm)
AEDC Tunnel 9	10	1.8×10^6	0.152
AEDC Tunnel 9	10	6.4×10^6	0.152
AEDC Tunnel 9	10	15.0×10^6	0.152
AEDC Tunnel 9	10	17.0×10^6	5.0
Sandia HWT	8	7.0×10^6	0.050

Prior to conducting the transition analysis, laminar base flows are computed using the fully non-linear SPARC code; that is, driving the right hand side of 3.41 to zero. The mesh used during this process is the same as the mesh used to simulate the instability waves, and therefore the grid resolution is more than sufficient to capture the details of the laminar flow.

5.3. Sharp Cones

5.3.1. Transition prediction validation

A comparison between our spatial optimization method and several sharp cone experiments is made in this section. To make an apt comparison, our solution method is to constrain our inflow using the measured freestream power spectra in Figure 5-1(b). To predict the location of transition, we use the minimum of the data collected in the experiments for the threshold pressure fluctuation of transition in Figure 5-1(a). Once we have a converged solution, we calculate the root-mean-squared wall pressure fluctuation and calculate the location where this RMS pressure exceeds the threshold pressure fluctuation measured in Figure 5-1(a).

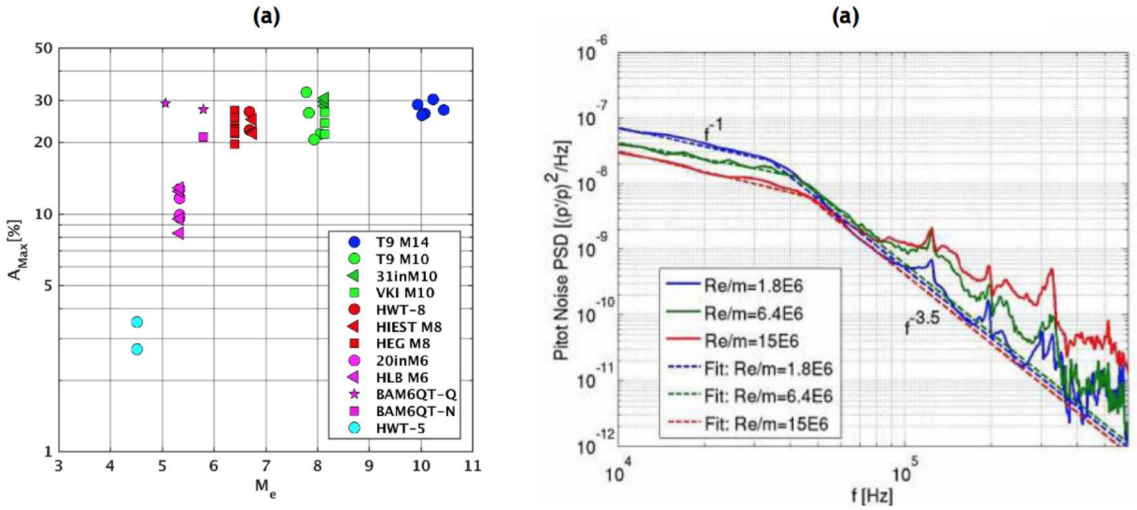

Figure 5-1. Experimental measurements of (a) Transition threshold pressure Marineau et al. [17] used to predict transition location, (b) Pressure power spectra at inflow used to constrain inflow optimization problem Marineau et al. [16].

The results of our comparison of the four different experiments is shown in Figure 5-2. In Figures 5-2(a,c) we fall within the experimental range of transition (red lines) for both experiments. In Figures 5-2(b,d), we slightly over-predict the transition location (we observe faster energy growth than the experiments), but our prediction still falls within an acceptable range. In all, the comparisons show that our spatial optimization method works well in predicting the transition location of 2nd mode disturbances when compared to experiments on sharp cones

In Figure 5-3, we compare the experimental results with the STABL (Stability and Transition Analysis for hypersonic Boundary Layers) transition prediction software. Here we compute the

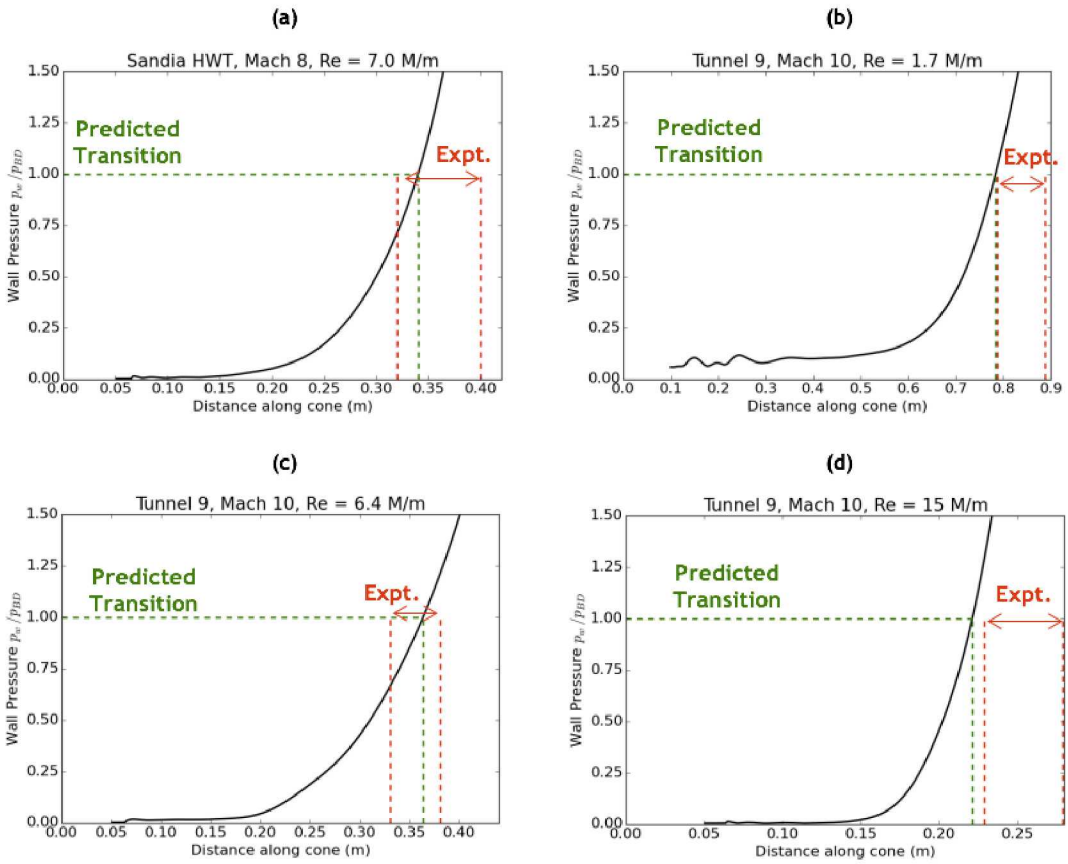

Figure 5-2. Comparison of optimized wall pressure RMS measurements compared to experiment Casper et al. [4], Marineau et al. [15] for (a) Sandia HWT $M = 8$ and $Re = 7 \times 10^6/m$. (b) Tunnel 9 $M = 10$ and $Re = 1.7 \times 10^6/m$. (c) Tunnel 9 $M = 10$ and $Re = 6.4 \times 10^6/m$. (d) Tunnel 9 $M = 10$ and $Re = 15 \times 10^6/m$.

"N" factor $N \approx ln(p_w/p_{w,i})$ where p_w is the wall presure fluctuation and $p_{w,i}$ is the wall pressure at the neutral point as calculated in STABL. Transition is said to occur at some threshold "N" factor (e.g. some expected growth of disturbance pressure). In this case, we fit the solution obtained from STABL to match the transition location for the HWT experiment (shown in Figure 5-3(a)). This computed N factor was selected as $N \approx 5.4$ and then used in the rest of the comparisons to the Tunnel 9 experiments. This is a typical method of predicting transition location using LST software. It can be seen that STABL has a difficult time correctly predicting transition. Sometimes it under-predicts the energy growth and doesn't even transition (Figure 5-3(b)), or over-predicts the energy growth an transitions too early (Figure 5-3(d)). It is noteworthy that N factor at transition increases from 4.2 to 7.2 for the range of Tunnel 9 cases presented above, indicating that a constant N factor in the e^N method is not accurate for this wind tunnel and flow field. The current transition method, on the other hand, captures the "unit Reynolds number" effect by accounting for the freestream noise levels. In any case, the ability of traditional methods (N factor correlations) to predict transition locations compared to experiments is lacking when compared to our optimization model.

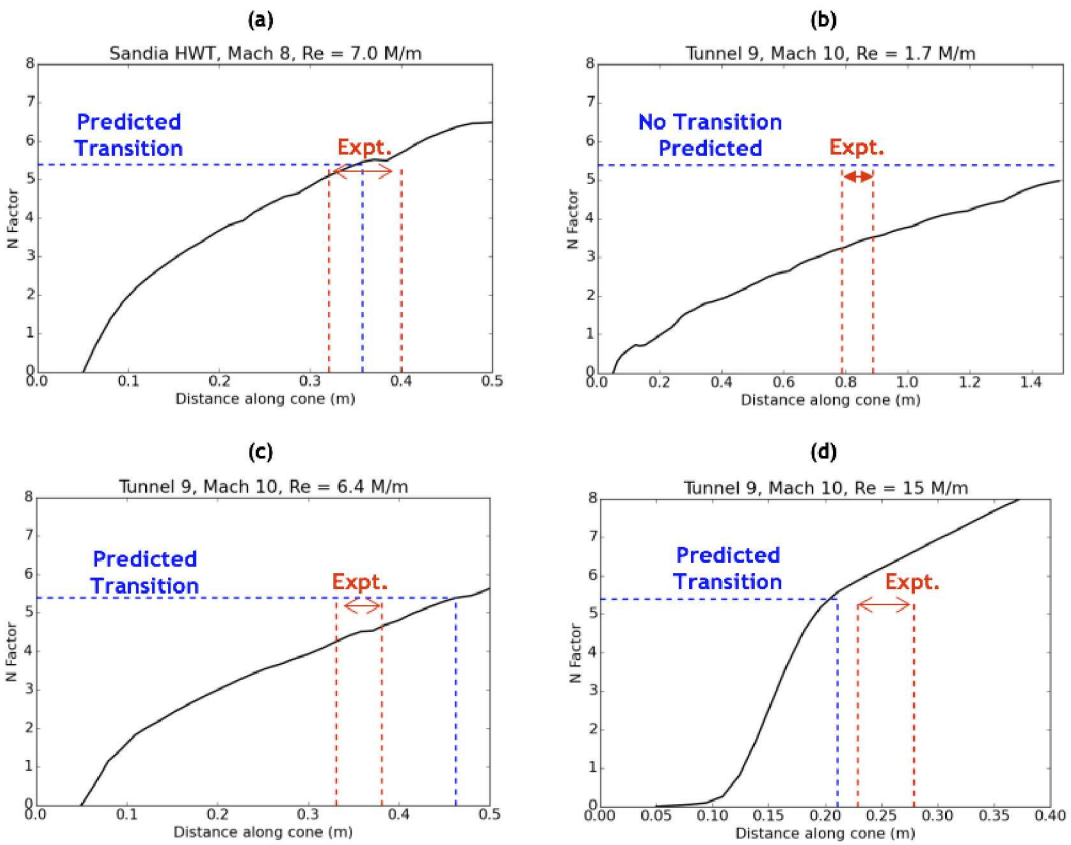

Figure 5-3. Comparison of STABL to predict transition using N-factor $N = 5.4$ (chosen to match Sandia HWT results) for (a) Sandia HWT $M = 8$ and $Re = 7 \times 10^6/m$. (b) Tunnel 9 $M = 10$ and $Re = 1.7 \times 10^6/m$. (c) Tunnel 9 $M = 10$ and $Re = 6.4 \times 10^6/m$. (d) Tunnel 9 $M = 10$ and $Re = 15 \times 10^6/m$.

5.3.2. Detailed transition data

To highlight some key features of the transition prediction method, the Mach 10, sharp cone experiment at a Reynolds number of 1.8×10^6 m^{-1} is described in detail. Figure 5-4 shows the variation of the magnitude of wall pressure with distance along the cone for several different frequencies. An example of the full pressure field corresponding to 80 kHz is shown in Figure 5-5. In this image, the contour levels are set to 0.05 times the maximum pressure on the inflow boundary so that the details of the flow field are visible (although the contour levels corresponding to the boundary layer instability are saturated). Interaction between the instability wave and the oblique shock is visible. It should be noted that this method does not include perturbation of the shock location, as is often done when treating shock-disturbance interactions [18]. However, despite being linearized, the current method uses exactly the same numerical schemes as a shock capturing finite volume code and thus the ability of our method to handle shock-disturbance interactions is identical to that of standard finite volume code (see, for example, Chaudhry and Candler [6, 7]).

A comparison between the measured RMS of surface pressure fluctuations from several sensors in the experiment to the calculated data show good agreement along the cone, shown in

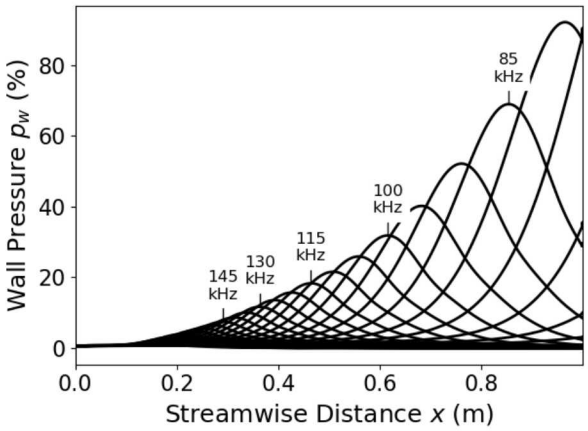

Figure 5-4. Wall pressure flucutation magnitude for different frequencies against initial wall amplitude.

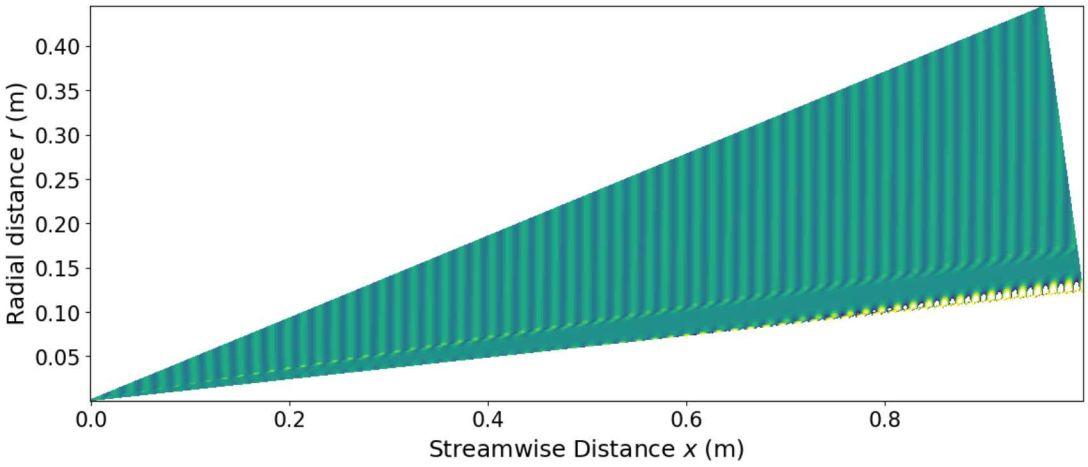

Figure 5-5. Pressure contours for 80 kHz. Maximum contour level is set to 0.05 times the maximum pressure at the inflow boundary to show flow field structure.

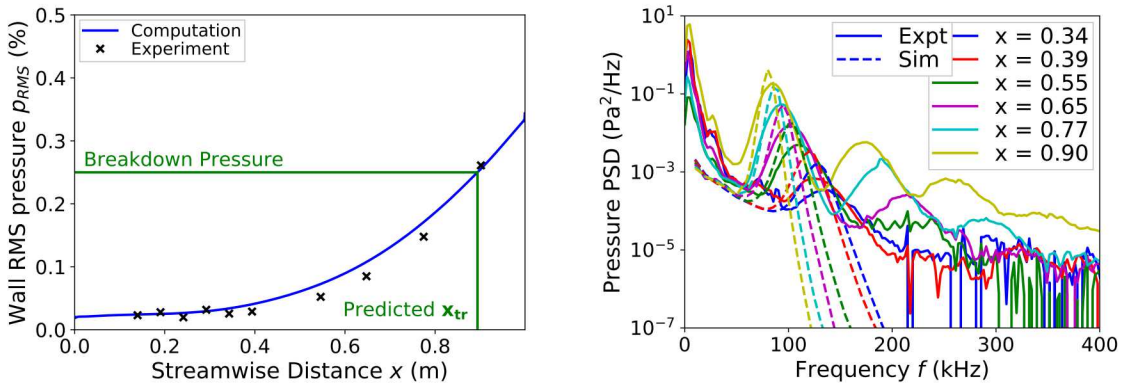

Figure 5-6. a) RMS pressure distribution along cone surface with predicted transition location. b) Comparison between measured and simulated pressure spectra at wall surface.

Figure 5-6a. In this figure, a threshold value from the middle of the breakdown range from Figure 5-1, 25%, is used to estimate the transition location. With this value, the predicted transition location of $x_{tr} = 0.89$ m determined by RMS pressure exceeding the breakdown threshold lies on the downstream end of the measured transition window, comparing favorably with the center of experimentally measured window of $x_{tr} = 0.84$ m [15].

While it is encouraging to match the RMS value of the surface pressure fluctuations, it is important to also verify that frequency range of the disturbances accurately reflects those generated in the wind tunnel. This is accomplished by comparing the PSD's of surface pressure fluctuation at several different sensors on the body, shown in figure Figure 5-6b. As seen in the figure, the most amplified frequency calculated with the current method lies within close proximity to measure value for several different sensors. The peak PSD value calculated at each location lies higher than the measured value, while the bandwidth of amplified frequencies is narrower than the measure bandwidth. The latter characteristic is common in modern stability analysis calculations in that the bandwidth discrepancy between experiments and computations has yet to be explained. The combination of a higher peak with a smaller bandwidth results in a similar RMS value shown in figure Figure 5-6a. However, the agreement between the calculation and the experiment in the PSDs is good.

Optimized vs not optimized

To quantify the value of optimizing the inflow boundary condition, flow over the cone is simulated using a variety of imposed boundary conditions, as well as the optimized boundary condition determined by the input/output analysis. Five sets of imposed boundary conditions are considered. The first four are two dimensional vorticity waves, entropy waves, slow acoustic waves, and fast acoustic waves, all traveling parallel to the cone axis. The fifth imposed boundary condition is a slow acoustic wave that is oblique with wavefronts oriented 60° to the cone axis.

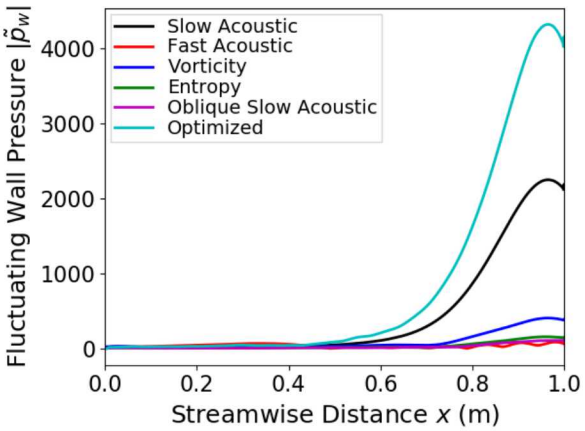

Figure 5-7. Comparison of wall pressure for 80 kHz waves with different types of freestream forcing.

Figure 5-7 compares the resulting wall pressure distribution from all of these different types of forcings for an 80 kHz forcing. In all cases, the waves at each point along the inflow boundary are normalized to have an energy of 1.0 according to the Mack energy norm. This normalization is used, as opposed to normalizing the pressure, because vorticity and entropy waves do not have a pressure component. As shown in the figure, for different types of waves having identical fluctuating energy, slow acoustic waves oriented along the cone axis are much more efficient at exciting boundary layer instabilities than oblique waves or vorticity/entropy waves. Very similar behavior is observed if the fluctuating energy in the boundary layer is plotted instead of the pressure at the wall. The optimized inflow disturbance is even more efficient than the slow acoustic wave, producing about twice the fluctuating amplitude in the boundary layer as the slow acoustic wave.

5.4. Blunt Cones

The results just presented are typical of sharp cones; for these geometries the slow acoustic wave parallel to the cone axis is highly effective at exciting boundary layer instabilities and thus captures the transition behavior observed in wind tunnels. On the other hand, for blunt cones the slow acoustic wave is not as close to optimal. As a result, transition predictions based on slow acoustic waves, as conducted by Balakumar and Chou [3], predict transition too late. In that paper, simulations of slow acoustic waves passing over the cone were conducted with wave amplitudes that matched the wind tunnel spectrum, similar to the approach used here. Transition was predicted using RMS amplitudes in the same manner used here, but the predicted transition location was far behind that which was observed in the experiment.

In this work, we allow the optimization procedure to select the type of disturbance flowing over the model. Figure 5-8 compares the wall pressure fluctuation obtained using the optimized disturbance to that of a slow acoustic wave. The Mack energy norm of the inflow is equal to 1.0 in both cases at every inflow cell. In this case the data is plotted on a logarithmic scale for clarity. At

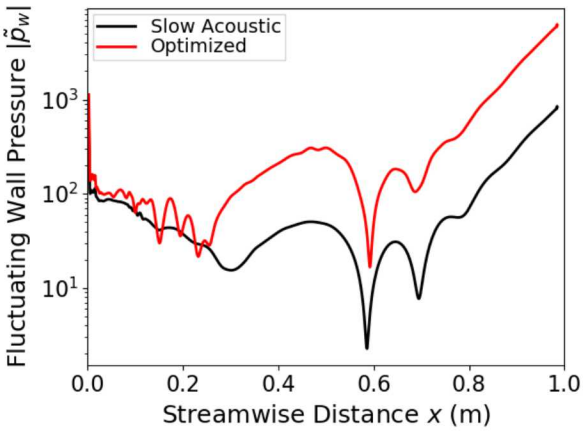

Figure 5-8. Comparison of wall pressure for 210 kHz waves with different types of freestream forcing

the aft end of the cone, the same slope is seen, indicating that both types of forcing are exciting the same instability mode with the same growth rate. However, the optimized case exhibits a large increase in between $0.2 < x < 0.4$ m which boosts the overall amplitude of the instability by more than an order of magnitude.

To better understand the performance of the current method a comparison is made to the simulations of Balakumar and Chou, shown in Figure 5-9, In this figure, Balakumar and Chou's DNS data are plotted as a snapshot, thus showing the full value of pressure across the wavelength of the disturbance wave. The PSE calculation and the current method only plot the maximum of the fluctuation pressure along the surface. As seen in the figure, current simulations have a 2nd mode neutral point further downstream than Balakumar and Chou. The cause for this is currently undetermined. However, the first half of the cone compares well to Balakumar and Chou. This confirms that our method adequately handles the shock-disturbance interactions, since the comparison results were conducted using an unsteady, weighted essentially non-oscillatory (WENO) scheme that fully captures the non-linearities present at the shock.

For the first part of the cone, the optimized disturbance maintains a higher value of pressure than that of the slow acoustic simulations. This difference in amplitude could explain the inability of the slow acoustic method to capture the transition behavior of the blunt cone case. To demonstrate the difference between the slow acoustic inflow and the optimized inflow, the pressure fluctuation contours are shown in Figure 5-10. While the optimized disturbance, in Figure 5-10b, is similar to the plane wave of the slow acoustic case, in Figure 5-10a, the optimized disturbance excites a significant portion of the forward shock layer.

Figure 5-9 also shows results from the current simulations using several different mesh sizes. The comparison of these results shows that the 12000x200 grid is sufficiently grid resolved. Similar grid convergence checks have been carried out for the other simulations reported in this paper.

To predict the transition location using the wall RMS pressure, thirty-two frequencies are sampled between 100 kHz to 300 kHz. The simulation and experimental RMS pressure is shown in Figure 5-11a. Following the analysis presented in the sharp cone section, it is assumed that the

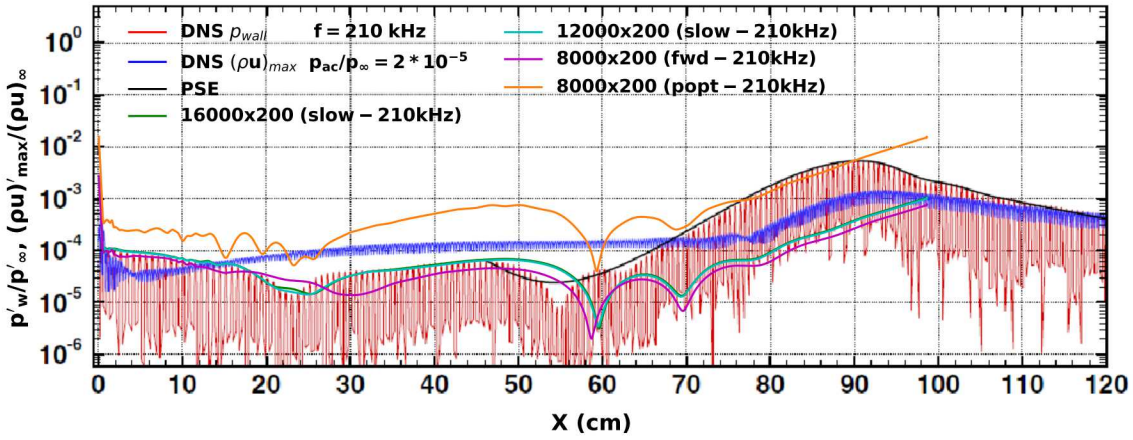

Figure 5-9. Comparison of wall pressure fluctuations from current simulations with those of Figure 14 in Balakumar and Chou [3].

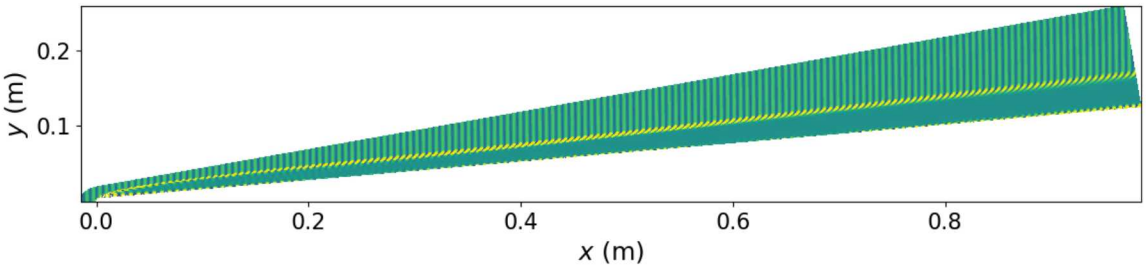

a) Slow acoustic wave simulation

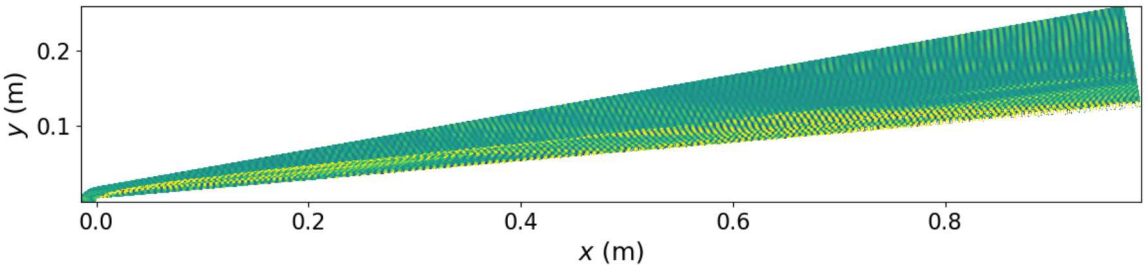

b) Optimized disturbance simulation

Figure 5-10. Comparison of the pressure fluctuations between the slow acoustic (a) and optimized disturbance (b) simulations on the blunt cone.

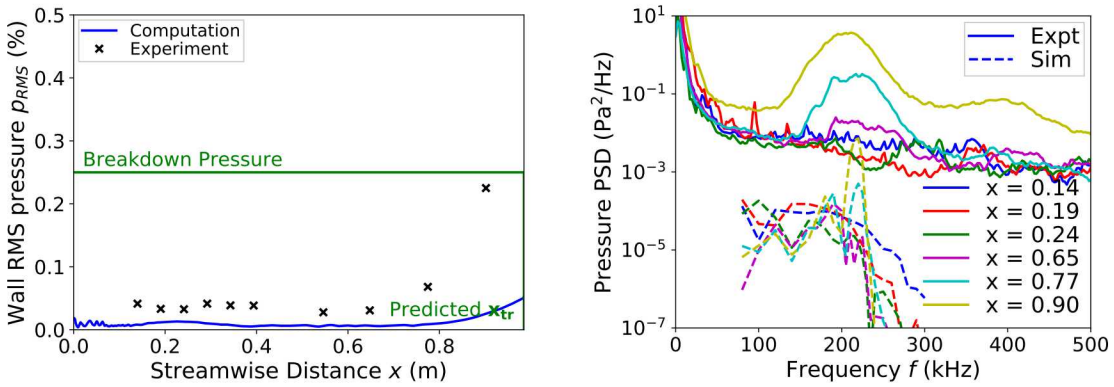

Figure 5-11. (a) RMS pressure distribution along the cone surface. (b) Comparison between measured and simulated pressure spectra at wall surface[15].

transition occurs at a breakdown threshold of 25%. In this case, the simulation fails to reproduce the experimental data points. This could be due to insufficient mesh resolution causing numerical dissipation. Another possible explanation for this discrepancy is that thirty-two frequency samples is not enough to converge to the true RMS pressure. Remember, the RMS pressure fluctuations is calculated by integrating the frequency samples power spectrum. As a result, it is likely that more frequency samples are necessary to improve the RMS pressure, which will lead to a viable transition prediction.

A comparison between experimental measurement and simulation pressure spectra at the surface is shown in Figure 5-11b. The calculated surface pressure deviates from the measured values by two orders of magnitude, however, the peak frequency agrees well. This is generally an indication that the base state reasonably matches the experiment and the the grid resolution may be insufficient where the disturbances are amplifying. As with the previous case, the simulation shows a narrower frequency band peak when compared to the experimental data from Marineau et al. [15].

6. CONCLUSION AND FUTURE STEPS

A new computational method for predicting laminar-turbulent boundary layer transition was developed and presented. The method has several advantages over the current state-of-the-practice, which uses empirical correlations, by directly computing disturbance amplification using the compressible Navier-Stokes equations. This allows for general application of the method rather than one confined to a specific geometry and flight condition and for continued confidence with the inclusion of other vehicle surface temperatures and ablation. The method also has advantages over the current state-of-the-art, which uses a linear stability analysis, by relieving some of the effort of subject matter experts through optimization of disturbance growth as well as an embedded solver within the framework of the CFD code that generates the base flow field. Additionally, this method is able to compute disturbance receptivity, thus allowing for an reliable means of predicting transition over freestream noise levels ranging from conventional wind tunnels to quiet wind tunnels to flight. Lastly, the method does not make any restricting assumptions, as is common in stability analysis, and should be capable of computing transition due to complex transition mechanisms on complex, 3D shapes.

In the paper, the optimization method was derived and details were provided about the implemention within a CFD code. The method was verified in code by demonstrating the optimization process by calculating an optimal disturbance for various scenarios involving flow over a flat plate. Next, the approach was validated by computing the transition location on sharp cones in two different wind tunnels and across four different flow conditions. The current method outperformed stability analysis in predicting the experimental transition location.

The method was also evaluated on a blunt cone. While there remains some work to replicate previous simulations as well as better match the measured transition location, the method showed promise in explaining the reason acoustic wave simulations were unable to properly predict the measured transition location.

From a practical perspective, the spatial method proved to be more useful for the current work. The convective instabilities considered in this paper are easier to simulate with a boundary condition that grows through space, rather than properly timing when a particular initial condition would achieve its greatest amplitude in simulation. As mention previously, the temporal method is required for properly modeling absolute instabilities. In those cases, the temporal method is predicted to be more useful.

One issue that was not explored in the paper is the question of realizability of the optimal disturbance. The method was able to demonstrate the ability to restrict the origin of a disturbance to the freestream, whether or not such a disturbance could exist in the freestream has yet to be determined. It is promising to see the increased pressure amplitude of the optimal disturbance in the blunt cone case as compared to the acoustic case. However, one must be cautious in applying

this method when it computes an input disturbance that cannot occur in the physical world. This is an issue that will be addressed in future work, when the method is more mature.

Additional future work for this transition prediction method includes application to cones at non-zero angles of attack, flight transition cases, and complex 3D geometries. The extension to three dimensions naturally occurs in the formulation of the method. However, the additional dimension adds a significant computational cost as well as increased complexity due to the increase in volume over which disturbances could potentially amplify. The scalability of the linear system solver will be stressed as the complexity of the flowfield increases and the physical model will be stressed as the flow enthalpy increases to flight cases.

REFERENCES

[1] S. Bagheri, E. Åkervik, L. Brandt, and D. S. Henningson. Matrix-free methods for the stability and control of boundary layers. *AIAA Journal*, 47(5):1057–1068, 2009.

[2] P. Balakumar. Receptivity of hypersonic boundary layers to acoustic and vortical disturbances. In *Proceedings of the 45th AIAA Fluid Dynamics Conference*, Dallas, TX, 2015. AIAA-2015-2473.

[3] P. Balakumar and A. Chou. Transition prediction in hypersonic boundary layers using receptivity and freestream spectra. *AIAA Journal*, 56(1):193–208, 2018.

[4] K. M. Casper, S. J. Beresh, J. F. Henfling, R. W. Spillers, B. O. M. Pruett, and S. P. Schneider. Hypersonic wind-tunnel measurements of boundary-layer transition on a slender cone. *AIAA Journal*, 54(4):1250–1263, 2016.

[5] C.L. Chang, H. Vinh, and M.R. Malik. Hypersonic boundary-layer stability with chemical reactions using PSE. In *Proceedings of the 28th AIAA Fluid Dynamics Conference*, Snowmass Village, CO, 1997. AIAA-97-2012.

[6] R. S. Chaudhry and G. V. Candler. Computing measured spectra from hypersonic pitot probes with flow-parallel freestream disturbances. *AIAA Journal*, 55(12):4155–4166, 2017.

[7] R. S. Chaudhry and G. V. Candler. Computations of measured pitot-probe spectra using angled freestream disturbances and comparison to experiments. In *AIAA Scitech 2019 Forum*, San Diego, CA, 2019. AIAA-2019-2149.

[8] David Day and Michael A. Heroux. Solving complex-valued linear systems via equivalent real formulations. *SIAM Journal on Scientific Computing*, 23(2):480–498, 2001. doi: 10.1137/S1064827500372262.

[9] A. H. Gebremedhin, F. Manne, and A. Pothen. What color is your jacobian? graph coloring for computing derivatives. *SIAM Review*, 47(4):629–705, 2005.

[10] F. Gomez, S. Le Clainche, P. Paredes, M. Hermanns, and V. Theofilis. Four decades of studying global linear instability: problems and challenges. *AIAA Journal*, 50(12), 2012.

[11] F. Gomez, R. Gomez, and V. Theofilis. On three-dimensional global linear instability analysis of flows with standard aerodynamics codes. *Aerospace Science and Technology*, 32: 223–234, 2014.

[12] H.B. Johnson and G.V. Candler. Hypersonic boundary layer stability analysis using pse-chem. 2005. AIAA Paper No. 2005-5023.

[13] H.B. Johnson, T.G. Seipp, and G.V. Candler. Numerical study of hypersonic reacting boundary layer transition on cones. In *Proceedings of the 32nd AIAA Thermophysics Conference*, Atlanta, GA, 1997. AIAA-97-2567.

[14] M. R. Malik. Stability theory for chemically reacting flows. In D. Arnal and R. Michel, editors, *Laminar-Turbulent Transition*, pages 251–260. IUTAM Symposium Toulouse/France, September 1989.

[15] E. C. Marineau, G. Moraru, D. R. Lewis, J. D. Norris, J. F. Lafferty, R. M. Wagnild, and J. A. Smith. Mach 10 boundary-layer transition experiments on sharp and blunted cones. In *Proceedings of the 19th AIAA International Space Planes and Hypersonic Systems and Technologies Conference*, Atlanta, GA, 2014. AIAA-2014-3108.

[16] E. C. Marineau, C. G. Moraru, D. R. Lewis, J. D. Norris, J. F. Lafferty, and H. B. Johnson. Investigation of Mach 10 boundary layer stability of sharp cones at angle-of-attack, part 1: Experiments. In *Proceedings of the 53rd AIAA Aerospace Sciences Meeting*, Kissimmee, Florida, 2015. AIAA-2015-1737.

[17] E. C. Marineau, G. Grossir, A. Wagner, M. Leinemann, R. Radespiel, H. Tanno, R. M. Wagnild, and K. M. Casper. Compilation of analysis of second-mode amplitudes on sharp cones in hypersonic wind tunnels. In *Proceedings of the 2018 Aerospace Sciences Meeting*, Kissimmee, FL, 2018. AIAA=2018-0349.

[18] J. F. McKenzie and K. O. Westphal. Interaction of linear waves with oblique shock waves. *Physics of Fluids*, 11(11):2350–2362, 1968.

[19] A. Monokrousos, E. Åkervik, L. Brandt, and D. S. Henningson. Global three-dimensional optimal disturbances in the blasius boundary-layer flow using time-steppers. *Journal of Fluid Mechanics*, 650:181–214, 2010.

[20] Sandia National Laboratories. Trilinos. https://trilinos.github.io, 2020. Accessed: 2020-01-01.

7. APPENDIX: STABILITY EQUATIONS

7.1. Continuity equation

The full continuity equation is:

$$\frac{\partial \rho}{\partial t} + u\frac{\partial \rho}{\partial x} + v\frac{\partial \rho}{\partial y} + \rho\left(\frac{\partial u}{\partial x} + \frac{\partial v}{\partial y}\right) = 0 \tag{7.1}$$

The linearized version is:

$$\frac{\partial \tilde{\rho}}{\partial t} + \bar{u}\frac{\partial \tilde{\rho}}{\partial x} + \bar{v}\frac{\partial \tilde{\rho}}{\partial y} + \tilde{u}\frac{\partial \bar{\rho}}{\partial x} + \tilde{v}\frac{\partial \bar{\rho}}{\partial y} + \bar{\rho}\left(\frac{\partial \tilde{u}}{\partial x} + \frac{\partial \tilde{v}}{\partial y}\right) + \tilde{\rho}\left(\frac{\partial \bar{u}}{\partial x} + \frac{\partial \bar{v}}{\partial y}\right) = 0 \tag{7.2}$$

7.2. X Momentum Equation

The full x momentum equation is:

$$\rho\left(\frac{\partial u}{\partial t} + u\frac{\partial u}{\partial x} + v\frac{\partial u}{\partial y}\right) + \frac{\partial p}{\partial x} = \frac{\partial}{\partial x}\left[(2\mu+\lambda)\frac{\partial u}{\partial x} + \lambda\frac{\partial v}{\partial y}\right] + \frac{\partial}{\partial y}\left[\mu\left(\frac{\partial u}{\partial y} + \frac{\partial v}{\partial x}\right)\right] \tag{7.3}$$

The linearized version is:

$$\begin{aligned}
\bar{\rho}\left(\frac{\partial \tilde{u}}{\partial t} + \bar{u}\frac{\partial \tilde{u}}{\partial x} + \bar{v}\frac{\partial \tilde{u}}{\partial y} + \tilde{u}\frac{\partial \bar{u}}{\partial x} + \tilde{v}\frac{\partial \bar{u}}{\partial y}\right) + \tilde{\rho}\left(\bar{u}\frac{\partial \bar{u}}{\partial x} + \bar{v}\frac{\partial \bar{u}}{\partial y}\right) + \frac{\partial \tilde{p}}{\partial x} = \\
(2\bar{\mu}+\bar{\lambda})\frac{\partial^2 \tilde{u}}{\partial x^2} + (\bar{\mu}+\bar{\lambda})\frac{\partial^2 \tilde{v}}{\partial x \partial y} + \bar{\mu}\frac{\partial^2 \tilde{v}}{\partial y^2} \\
+\left(2\frac{\partial \bar{\mu}}{\partial x} + \frac{\partial \bar{\lambda}}{\partial x}\right)\frac{\partial \tilde{u}}{\partial x} + \frac{\partial \bar{\mu}}{\partial y}\frac{\partial \tilde{v}}{\partial x} + \frac{\partial \bar{\mu}}{\partial y}\frac{\partial \tilde{u}}{\partial y} + \frac{\partial \bar{\lambda}}{\partial x}\frac{\partial \tilde{v}}{\partial y} \\
+\left[\left(2\frac{\partial \mu}{\partial T} + \frac{\partial \lambda}{\partial T}\right)\frac{\partial^2 \bar{u}}{\partial x^2} + \left(\frac{\partial \mu}{\partial T} + \frac{\partial \lambda}{\partial T}\right)\frac{\partial^2 \bar{v}}{\partial x \partial y} + \frac{\partial \mu}{\partial T}\frac{\partial^2 \bar{u}}{\partial y^2}\right]\tilde{\theta} \\
2\frac{\partial \bar{u}}{\partial x}\left(\frac{\partial \mu}{\partial T}\frac{\partial \tilde{\theta}}{\partial x} + \frac{\partial^2 \mu}{\partial T^2}\frac{\partial \bar{T}}{\partial x}\tilde{\theta}\right) + \left[\frac{\partial \bar{u}}{\partial x} + \frac{\partial \bar{v}}{\partial y}\right]\left(\frac{\partial \lambda}{\partial T}\frac{\partial \tilde{\theta}}{\partial x} + \frac{\partial^2 \lambda}{\partial T^2}\frac{\partial \bar{T}}{\partial x}\tilde{\theta}\right) \\
+\left[\frac{\partial \bar{u}}{\partial y} + \frac{\partial \bar{v}}{\partial x}\right]\left(\frac{\partial \mu}{\partial T}\frac{\partial \tilde{\theta}}{\partial y} + \frac{\partial^2 \mu}{\partial T^2}\frac{\partial \bar{T}}{\partial y}\tilde{\theta}\right)
\end{aligned} \tag{7.4}$$

7.3. Y Momentum Equation

The full y momentum equation is:

$$\rho\left(\frac{\partial v}{\partial t}+u\frac{\partial v}{\partial x}+v\frac{\partial v}{\partial y}\right)+\frac{\partial p}{\partial y}=\frac{\partial}{\partial x}\left[\mu\left(\frac{\partial v}{\partial x}+\frac{\partial u}{\partial y}\right)\right]+\frac{\partial}{\partial y}\left[(2\mu+\lambda)\frac{\partial v}{\partial y}+\lambda\frac{\partial u}{\partial x}\right] \tag{7.5}$$

The linearized version is:

$$\begin{aligned}\bar{\rho}\left(\frac{\partial \tilde{v}}{\partial t}+\bar{u}\frac{\partial \tilde{v}}{\partial x}+\bar{v}\frac{\partial \tilde{v}}{\partial y}+\tilde{u}\frac{\partial \bar{v}}{\partial x}+\tilde{v}\frac{\partial \bar{v}}{\partial y}\right)+\tilde{\rho}\left(\bar{u}\frac{\partial \bar{v}}{\partial x}+\bar{v}\frac{\partial \bar{v}}{\partial y}\right)+\frac{\partial \tilde{p}}{\partial y}= \\ \bar{\mu}\frac{\partial^2 \tilde{v}}{\partial x^2}+(\bar{\mu}+\bar{\lambda})\frac{\partial^2 \tilde{u}}{\partial x\partial y}+(2\bar{\mu}+\bar{\lambda})\frac{\partial^2 \tilde{v}}{\partial y^2} \\ +\frac{\partial^2 \bar{v}}{\partial x^2}\frac{\partial \mu}{\partial T}\tilde{\theta}+\frac{\partial^2 \bar{u}}{\partial x\partial y}\left(\frac{\partial \mu}{\partial T}+\frac{\partial \lambda}{\partial T}\right)\tilde{\theta}+\frac{\partial^2 \bar{v}}{\partial y^2}\left(2\frac{\partial \mu}{\partial T}+\frac{\partial \lambda}{\partial T}\right)\tilde{\theta} \\ +\frac{\partial \bar{\mu}}{\partial x}\frac{\partial \tilde{v}}{\partial x}+\frac{\partial \bar{\mu}}{\partial x}\frac{\partial \tilde{u}}{\partial y}+\left(2\frac{\partial \bar{\mu}}{\partial y}+\frac{\partial \bar{\lambda}}{\partial y}\right)\frac{\partial \tilde{v}}{\partial y}+\frac{\partial \bar{\lambda}}{\partial y}\frac{\partial \tilde{u}}{\partial x} \\ +2\frac{\partial \bar{v}}{\partial y}\left(\frac{\partial \mu}{\partial T}\frac{\partial \tilde{\theta}}{\partial y}+\frac{\partial^2 \mu}{\partial T^2}\frac{\partial \bar{T}}{\partial y}\tilde{\theta}\right)+\left(\frac{\partial \bar{u}}{\partial x}+\frac{\partial \bar{v}}{\partial y}\right)\left(\frac{\partial \lambda}{\partial T}\frac{\partial \tilde{\theta}}{\partial y}+\frac{\partial^2 \lambda}{\partial T^2}\frac{\partial \bar{T}}{\partial y}\tilde{\theta}\right) \\ +\left(\frac{\partial \bar{v}}{\partial x}+\frac{\partial \bar{u}}{\partial y}\right)\left(\frac{\partial \mu}{\partial T}\frac{\partial \tilde{\theta}}{\partial x}+\frac{\partial^2 \mu}{\partial T^2}\frac{\partial \bar{T}}{\partial x}\tilde{\theta}\right)\end{aligned} \tag{7.6}$$

$$\tag{7.7}$$

7.4. Energy Equation

The full energy equation is:

$$\rho C_v\left(\frac{\partial T}{\partial t}+u\frac{\partial T}{\partial x}+v\frac{\partial T}{\partial y}\right)+\rho RT\left(\frac{\partial u}{\partial x}+\frac{\partial v}{\partial y}\right)=\frac{\partial}{\partial x}\left(k\frac{\partial T}{\partial x}\right)+\frac{\partial}{\partial y}\left(k\frac{\partial T}{\partial y}\right)+\tau_{ij}\frac{\partial u_i}{\partial x_j} \tag{7.8}$$

The linearized version is:

$$
\begin{aligned}
\bar{\rho}C_v\left(\frac{\partial\tilde{\theta}}{\partial t}+\bar{u}\frac{\partial\tilde{\theta}}{\partial x}+\bar{v}\frac{\partial\tilde{\theta}}{\partial y}+\tilde{u}\frac{\partial\bar{T}}{\partial x}+\tilde{v}\frac{\partial\bar{T}}{\partial y}\right)+\tilde{\rho}C_v\left(\bar{u}\frac{\partial\bar{T}}{\partial x}+\bar{v}\frac{\partial\bar{T}}{\partial y}\right)\\
+\left(\bar{\rho}R\tilde{\theta}+\tilde{\rho}R\bar{T}\right)\left(\frac{\partial\bar{u}}{\partial x}+\frac{\partial\bar{u}}{\partial y}\right)+\bar{\rho}R\bar{T}\left(\frac{\partial\tilde{u}}{\partial x}+\frac{\partial\tilde{v}}{\partial y}\right)=\\
\bar{k}\left(\frac{\partial^2\tilde{\theta}}{\partial x^2}+\frac{\partial^2\tilde{\theta}}{\partial y^2}\right)+\frac{\partial k}{\partial T}\left(\frac{\partial^2\bar{T}}{\partial x^2}+\frac{\partial^2\bar{T}}{\partial y^2}\right)\tilde{\theta}+\frac{\partial\bar{k}}{\partial x}\frac{\partial\tilde{\theta}}{\partial x}+\frac{\partial\bar{k}}{\partial y}\frac{\partial\tilde{\theta}}{\partial y}\\
+\frac{\partial\bar{T}}{\partial x}\left(\frac{\partial k}{\partial T}\frac{\partial\tilde{\theta}}{\partial x}+\frac{\partial^2 k}{\partial T^2}\frac{\partial T}{\partial x}\tilde{\theta}\right)+\frac{\partial\bar{T}}{\partial y}\left(\frac{\partial k}{\partial T}\frac{\partial\tilde{\theta}}{\partial y}+\frac{\partial^2 k}{\partial T^2}\frac{\partial T}{\partial y}\tilde{\theta}\right)\\
+\bar{\tau}_{ij}\frac{\partial\tilde{u}_i}{\partial x_j}+\frac{\partial\bar{u}}{\partial x}\left[(2\mu+\lambda)\frac{\partial\tilde{u}}{\partial x}+\lambda\frac{\partial\tilde{v}}{\partial y}\right]+\frac{\partial\bar{u}}{\partial x}\left[\left(2\frac{\partial\mu}{\partial T}+\frac{\partial\lambda}{\partial T}\right)\frac{\partial\bar{u}}{\partial x}+\frac{\partial\lambda}{\partial T}\frac{\partial\bar{v}}{\partial y}\right]\tilde{\theta}\\
+\frac{\partial\bar{u}}{\partial y}\left[\bar{\mu}\left(\frac{\partial\tilde{u}}{\partial y}+\frac{\partial\tilde{v}}{\partial x}\right)+\frac{\partial\mu}{\partial T}\left(\frac{\partial\bar{u}}{\partial y}+\frac{\partial\bar{v}}{\partial x}\right)\tilde{\theta}\right]\\
+\frac{\partial\bar{v}}{\partial x}\left[\bar{\mu}\left(\frac{\partial\tilde{v}}{\partial x}+\frac{\partial\tilde{u}}{\partial y}\right)+\frac{\partial\mu}{\partial T}\left(\frac{\partial\bar{v}}{\partial x}+\frac{\partial\bar{u}}{\partial y}\right)\right]\\
+\frac{\partial\bar{v}}{\partial y}\left[(2\bar{\mu}+\bar{\lambda})\frac{\partial\tilde{v}}{\partial y}+\bar{\lambda}\frac{\partial\tilde{u}}{\partial x}+\left(2\frac{\partial\mu}{\partial T}+\frac{\partial\lambda}{\partial T}\right)\frac{\partial\bar{v}}{\partial y}\tilde{\theta}+\frac{\partial\lambda}{\partial T}\frac{\partial\bar{u}}{\partial x}\tilde{\theta}\right]
\end{aligned}
\tag{7.9}
$$

The equations of motion (2.2) can be linearized to produce the linearized Navier-Stokes equations:

$$\frac{\partial \tilde{\rho}}{\partial t} + \nabla \cdot (\bar{\mathbf{u}}\tilde{\rho} + \bar{\rho}\tilde{\mathbf{u}}) = 0 \tag{7.10}$$

$$\bar{\rho}\left(\frac{\partial \tilde{\mathbf{u}}}{\partial t} + \bar{\mathbf{u}} \cdot \nabla \tilde{\mathbf{u}} + \tilde{\mathbf{u}} \cdot \nabla \bar{\mathbf{u}}\right) + \tilde{\rho}\bar{\mathbf{u}} \cdot \nabla \bar{\mathbf{u}} + \nabla \tilde{p} = \nabla \cdot \tilde{\tau} \tag{7.11}$$

$$\bar{\rho} C_v \left(\frac{\partial \tilde{T}}{\partial t} + \bar{\mathbf{u}} \cdot \nabla \tilde{T} + \tilde{\mathbf{u}} \cdot \nabla \bar{T}\right) + \tilde{\rho} C_v \bar{\mathbf{u}} \cdot \nabla \bar{T} + \tilde{p} \nabla \cdot \bar{\mathbf{u}} + \bar{p} \nabla \cdot \tilde{\mathbf{u}} = \nabla \cdot \tilde{\mathbf{q}} + \tilde{\Phi} \tag{7.12}$$

DISTRIBUTION

Hardcopy—External

Number of Copies	Name(s)	Company Name and Company Mailing Address
1	Neal Bitter, JHU/APL	

Hardcopy—Internal

Number of Copies	Name	Org.	Mailstop
1	Ross M. Wagnild	1515	0825
1	Jeff A. Fike	1515	0825
1	Alec Kucala	1516	0828
1	Michael C. Krygier	1513	0825

Email—Internal (encrypt for OUO)

Name	Org.	Sandia Email Address
Technical Library	01177	libref@sandia.gov

Sandia National Laboratories is a multimission laboratory managed and operated by National Technology & Engineering Solutions of Sandia LLC, a wholly owned subsidiary of Honeywell International Inc., for the U.S. Department of Energy's National Nuclear Security Administration under contract DE-NA0003525.